Journal of
Materials Chemistry A

REVIEW

View Article Online
View Journal | View Issue

Cite this: *J. Mater. Chem. A*, 2025, **13**, 41555

A review on electrochemical CO_2-to-CH_4 conversion for a sustainable energy future: from electrocatalysts to electrolyzers

Javier Quílez-Bermejo * and Juan Herranz *

Received 13th May 2025
Accepted 3rd October 2025

DOI: 10.1039/d5ta03854e

rsc.li/materials-a

The electrochemical reduction of carbon dioxide (CO_2) to methane (CH_4) offers a promising route to renewable fuels and carbon circularity, addressing urgent climate and energy challenges. However, key bottlenecks such as limited selectivity, sluggish reaction kinetics, and insufficient long-term stability still hinder the practical deployment of this reaction and technology. Fundamental research has uncovered promising electrocatalysts and mechanistic insights to overcome these limitations, yet translating these advances into scalable industrial solutions remains a major challenge. This review addresses this critical gap by providing a comprehensive and focused overview of electrochemical CO_2-to-CH_4 conversion, from fundamental reaction mechanisms to system-level implementation. This work systematically analyzes the most selective and active electrocatalysts developed to date, elucidating key design principles that govern CH_4 production. In addition, we assess the evolution of CO_2 electrolyzers tailored for CH_4, comparing device configurations, operational strategies, and levels of technological maturity. Techno-economic evaluations are also integrated to identify bottlenecks and realistic near-term implementation scenarios. As the demand for green CH_4 rises at a pace that outstrips conventional CH_4 growth, this technology emerges as a timely solution to decarbonize hard-to-abate sectors using renewable electricity.

1 Introduction

The average atmospheric carbon dioxide (CO_2) concentration in 2024 has once again reached an unprecedented level of 422 ppm, surpassing all historical human records. Projections indicate that the 2025 annual average CO_2 concentration is expected to exceed a peak value of 427 ppm[1] for the first time in the last 800 000 years.[2] This trend is anticipated to continue in an upward trajectory in the coming years, and this high concentration of CO_2 in the atmosphere is already contributing to a substantial rise in global temperature,[3,4] ocean acidification[5] and the disruption of the carbon cycle.[6] This forces scientists to intensify their efforts to explore and develop environmentally friendly ways of energy production,[7] with a focus on technologies that should aim to either reduce or (ideally) fully replace the use of conventional fossil fuel-based methods.[8,9] Beyond this urgent need to foster the broad implementation of such renewable energy sources, short- to mid-term solutions require a decrease of non-abatable CO_2 emissions or even active strategies to capture atmospheric CO_2. To strengthen the economic viability of such approaches, CO_2 capture[10,11] should ideally be followed by the conversion of the carbon dioxide into value-added chemicals useful for industrial applications.[12,13] This CO_2 conversion encompasses different methods, including chemical conversion,[14–16] biological transformation,[17,18] photocatalytic reduction[19–21] and electrochemical reduction.[22–24]

These CO_2-conversion methods are plagued by well-known drawbacks, such as high energy requirements, low conversion rates, *etc.* By comparison, the electrochemical CO_2 reduction reaction (ECO_2RR) has recently emerged as a highly promising pathway due to the possibility of coupling it with renewable electricity, as pictured in Fig. 1.[25,26] Furthermore, some of the products of the ECO_2RR (*e.g.*, CO and C_2H_4) can serve as valuable fuels or chemicals that integrate perfectly into existing industrial processes. Moreover, this electrochemical reaction is well-known for its controllable and mild reaction conditions (*i.e.*, close-to-atmospheric temperatures and pressures). Nonetheless, there are still notable challenges associated with the ECO_2RR, including its limited operative current density (often $<< 1\ A\ cm^{-2}$), poor selectivity towards producing a single desired product, and lack of stability.[27–29]

In an industrial context, two different application scenarios are envisaged for the ECO_2RR. First, the reaction can be conducted within a standalone electrochemical system in which the resulting products are stored for subsequent use in other industries. Alternatively, the CO_2 can be electrochemically converted into a value-added product that is directly coupled to a second reactor, thus avoiding (or at least mitigating)

Paul-Scherrer-Institute, 5232 Villigen PSI, Switzerland. E-mail: javier.quilez-bermejo@psi.ch; juan.herranz@psi.ch

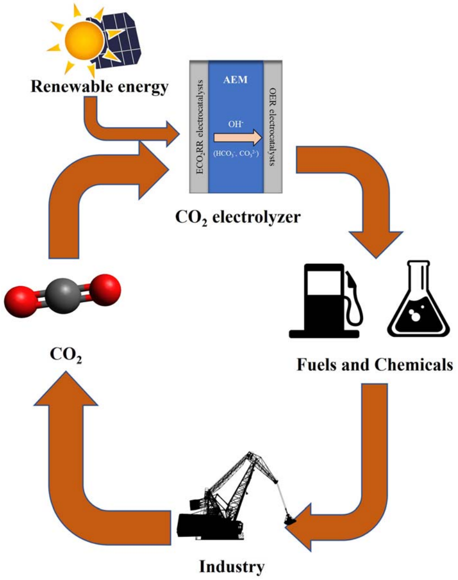

Fig. 1 Illustration of the closed carbon cycle enabled by a CO_2 electrolyzer (in this example, relying on the use of an anion exchange membrane, AEM, and with the O_2 evolution reaction (OER) as the anodic counter reaction) powered by renewable energy sources and that converts captured or emitted CO_2 into chemicals or fuels for their direct usage in the industrial sector.

additional costs associated with product storage and transportation. This second approach is more demanding in terms of performance because the resulting products must be of extremely high purity. Since they are fed directly into another industrial process, they need to meet strict quality standards to ensure efficiency and prevent any negative impact on the subsequent production state. This represents an important bottleneck in the ECO_2RR, as many materials electrochemically reduce CO_2 to a wide variety of carbon-containing chemicals and/or H_2 with poor selectivity.[30–32]

One of these possible ECO_2RR products is methane (CH_4), which has otherwise found extensive use as an energy source in the fields of low-pollution power generation, liquid-natural-gas vehicles and so on.[30] CH_4 is particularly valuable where existing infrastructure for natural gas storage, distribution and consumption can be leveraged,[23] since 70–90% of this natural gas (which is mainly obtained from oil wells and coal beds[33]) is composed of CH_4.[34] As an extensive storage and distribution network already exists for natural gas, the development of electrochemical CO_2-to-CH_4 conversion would enable a rapid and widespread distribution of net-zero-carbon energy services.[35,36] The global high purity methane gas market was valued at USD 101 billion in 2020 and is projected to reach USD 153 billion by 2025,[37] which is by far superior to other ECO_2RR-derived products, such as CO (USD 3.3 billion in 2022 and projected to reach USD 4.5 billion by 2030)[38] or HCOOH (USD 2.1 billion in 2023 and projected to reach USD 3.8 billion by 2030).[39] Nevertheless, several challenges impede the widespread implementation of electrochemical CO_2-to-CH_4 conversion, including the low faradaic efficiencies (FEs), sluggish kinetics and poor durability exhibited by most catalysts and reactor configurations. Moreover, the electrochemical production of CH_4 faces economic hurdles, as this gas possesses the lowest average market price among all CO_2-derived products.[40] Specifically, the cost of CH_4 from the electrochemical reduction of CO_2 is expected to stand at approximately 2.5–10 \$ kg^{-1}, which is still higher than traditional CH_4-synthesis methods (0.2–0.5 \$ kg^{-1}).[40] In this regard, technoeconomic analyses have suggested that the price of ECO_2RR-derived CH_4 must be reduced to at least $\approx$1.0 \$ kg^{-1} to effectively compete with traditional CH_4-production procedures.[40] Today, these elevated costs represent a major barrier for large-scale implementation, as achieving cost parity still requires substantial improvements in energy efficiency, catalyst durability, and system integration (or alternatively, stronger policy incentives to shift competitiveness). The successful integration of electrochemical CO_2-to-CH_4 conversion into existing natural gas infrastructure will strongly depend on consolidating the past achievements while addressing the remaining technoeconomic challenges.

With this motivation, in this review we comprehensively examine the advancements in electrochemical CO_2-to-CH_4 conversion, focusing on the nature of electrocatalysts and the design of electrochemical cells and devices. We first discuss the fundamental principles of the ECO_2RR, including reduction mechanisms and electric double layer (EDL) effects. Subsequently, we delve deeply into the recent developments concerning electrocatalysts, operating conditions and CO_2 electrolyzers. Finally, we offer insights into the future prospects of the ECO_2RR and highlight the challenges that must be addressed to enhance the efficiency and effectiveness of this electrochemical reaction to accomplish technoeconomic requirements.

2 Fundamentals of the ECO_2RR

2.1 Thermodynamics and reaction mechanism

CO_2 is a thermodynamically stable molecule with linear geometry and a dissociation energy of the C═O bond of $\approx$750 kJ mol^{-1}.[30,41] This high energy requirement suggests a substantial activation energy for direct C═O bond dissociation. In the CO_2 reduction mechanism, this activation must be considered as the first step, where the linear geometry of the pristine molecule is transformed into a bent configuration in which the C═O bond is weakened through the formation of chemical bonds between the CO_2 molecules and the active sites.[42] After CO_2 adsorption, the ECO_2RR goes through a series of reaction steps at the surface of the active phase involving the cleavage of C–O bonds, C–C coupling, or C–H formation, and multiple electron transfer processes (*e.g.*, 2 electrons for CO, 6 electrons for CH_3OH) and eventually leading to different products.[43,44]

In theory, this variety of ECO_2R reactions generally exhibits their thermodynamic equilibrium potentials at values close to 0.0 V *vs.* the reversible hydrogen electrode (RHE), as shown in Table 1, which also includes the competing (and undesired) H_2-

Table 1 Electrochemical CO_2 reduction potentials *versus* the standard hydrogen electrode (SHE) at pH 7. Hydrogen evolution reaction is included for comparison purposes

Electrochemical reaction	Thermodynamic potential/V *vs.* RHE
$CO_2 + 2H^+ + 2e^- \rightarrow HCOOH$	−0.12
$CO_2 + 2H^+ + 2e^- \rightarrow CO + H_2O$	−0.10
$CO_2 + 6H^+ + 6e^- \rightarrow CH_3OH + H_2O$	0.03
$CO_2 + 8H^+ + 8e^- \rightarrow CH_4 + 2H_2O$	0.17
$2CO_2 + 12H^+ + 12e^- \rightarrow C_2H_4 + 4H_2O$	0.08
$2H^+ + 2e^- \rightarrow H_2$	0.00

evolution reaction (HER). All potentials were calculated based on the Gibbs free energy of reaction, using gas-phase thermochemistry data and Henry's law data for aqueous products.[24] Beyond these thermodynamic considerations, one must bear in mind that large overpotentials are often required for achieving sufficiently high current densities due to the sluggish kinetics of these reactions.[45–47] Furthermore, the ECO_2RR is highly sensitive to the applied potential, as the selectivity towards a given product usually follows the tendency of increasing until a maximum value and then decreasing when more negative potentials are applied.

Concerning the electrochemical CO_2-to-CH_4 reduction reaction, it has been proposed that CH_4 formation undergoes two stages schematized in Fig. 2: the first one is the initial formation of a CO intermediate adsorbed to the catalyst surface (*CO) and one water molecule, and the second stage is the subsequent hydrogenation of the *CO into CH_4.[42,48] The key factor determining the selectivity towards CH_4 formation appears to be related to the binding energy of the *CO. Namely, if the binding energy of this intermediate is too weak, most of the *CO will desorb as carbon monoxide (CO), whereas a moderate binding energy between the active site and the C atom of the *CO intermediate is mandatory to reach high selectivity towards CH_4 formation. Computational studies have demonstrated that this hydrogenation can take place through (a) the hydrogenation of the C atom forming a so-called *CHO intermediate, or (b) the weakening of the C=O bond through the hydrogenation of the O atom, to form a *C–OH intermediate (see Fig. 2). The rate determining step in both mechanisms is the formation of the first hydrogenation intermediate (*i.e.*, *CHO or *COH). It is worth pointing out that the *COH intermediate might result in the formation of either CH_4 or CH_3OH, while *CHO can also proceed to form C_{2+} compounds. In pathway (b), water may be desorbed and lead to the ECO_2RR to proceed through a *C intermediate. After electron–proton pair additions, this intermediate undergoes reduction reactions towards *CH, *CH_2 and so on.[49]

There are also several competitive reactions that can tune the selectivity towards CH_4 formation from CO_2. In mechanism (a), the selectivity for CH_4 generation over CH_3OH is determined by the last reduction step, where *CH_2OH can undergo two different pathways leading to the hydrogenation of either the oxygen or the carbon atoms. At the same time, it has been demonstrated that C_2H_4 and CH_4 generation share similar pathways until the *CHO intermediate.[48] If C–C coupling reactions are favored at the electrocatalyst's surface, the formation

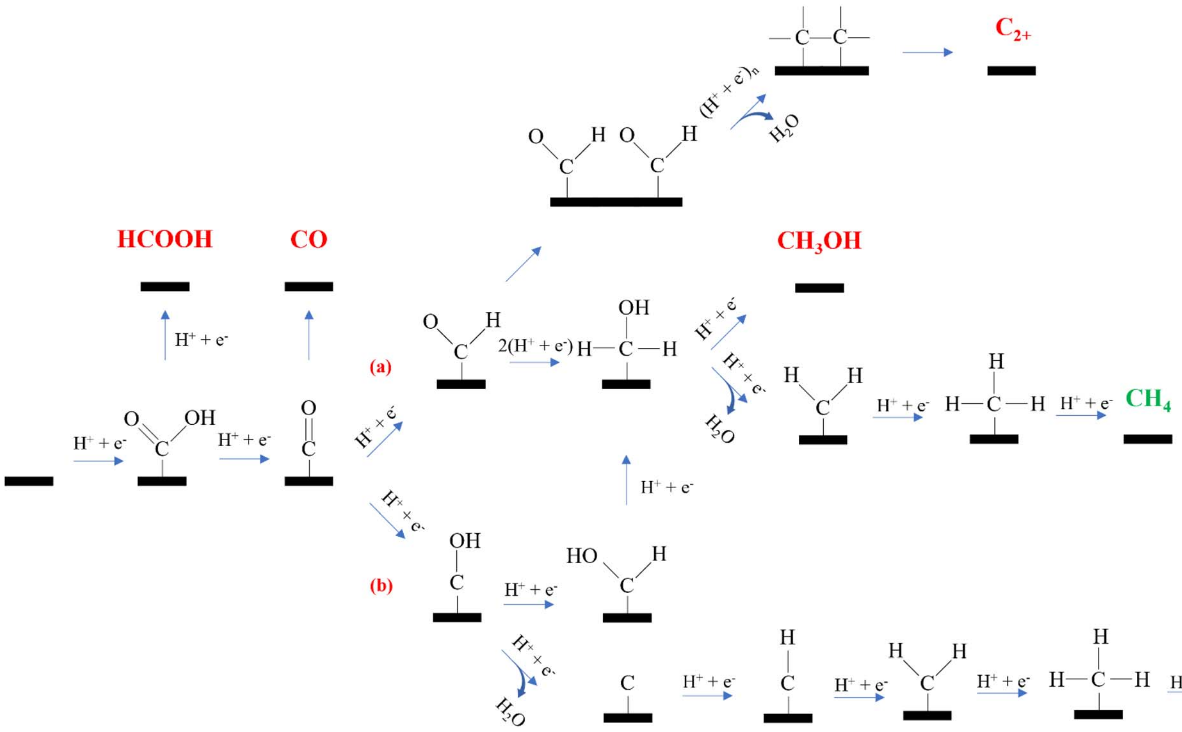

Fig. 2 Proposed mechanism for electrochemical CO_2-to-CH_4 conversion and competitive reactions towards other CO_2-derived products.

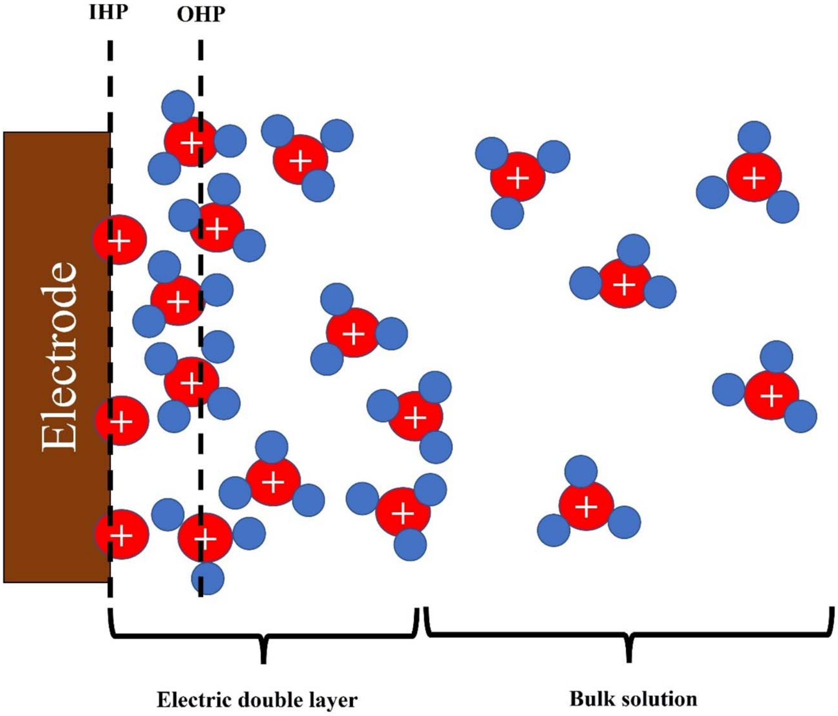

Fig. 3 Illustration of the inner Helmholtz plane (IHP) and outer Helmholtz plane (OHP) in the electric double layer. Red spheres represent the cation and blue spheres represent water molecules acting as solvation spheres. Anions in the solution are not incorporated for the sake of clarity.

of an OHC*–*CHO intermediate will predominate. Thus, in the search for highly selective CO_2-to-CH_4 electrocatalysts, the active sites should favor the completion of the CH_4 pathway avoiding C–C coupling.

The HER is the main competing reaction in the cathodic reduction of CO_2 in aqueous electrolytes, since it features a similar equilibrium potential (Table 1) and is particularly facile to catalyze in acid solutions.[47] The first reaction step involves the reduction of protons or H_2O molecules in the electrolyte to produce adsorbed H (H*, known as the Volmer step) that is subsequently further reduced to generate H_2 molecules. If the catalyst's active sites exhibit strong H* adsorption, the HER will predominate and the ECO_2RR will be suppressed, and thus a good ECO_2RR electrocatalyst must feature a weak binding strength towards H* and moderate CO_2 activation.

2.2 Electric double layer

Although the electrolyte is sometimes considered chemically inert in many electrochemical reactions, the identity of the ions present in it is known to affect the reaction rates and product selectivity of many electrochemical reactions in impactful ways.[50] This is in part due to the electric double layer (EDL) that forms when a solution containing ions is in contact with a solid surface that holds stationary charges.[51] The EDL is the result of the attractive and repulsive electrostatic interactions between the ions in the electrolyte and the charged surface, creating a locally varied electric potential. The understanding of the EDL in electrochemical reactions has significantly advanced over the decades. The proposed theories include (i) the blocking of the active sites by ions of the electrolyte, (ii) the redistribution of the potential drop in the double layer, which heavily affects the driving force for electron transfer, (iii) the interaction of the interfacial electric field with the electric dipole moments and polarizabilities of adsorbed intermediates, (iv) chemical interaction between ions and reaction intermediates, (v) the buffering of the interfacial pH by hydrated ions, and (vi) the alteration of the interfacial water structure.[52] To fully understand the EDL, it is worth mentioning that all these theoretical concepts are not strictly separable but interrelated.

For cathodic reactions like the ECO_2RR, the electrode is negatively polarized and its negative charge translates into an excess of cations and a depletion of anions in the vicinity of its surface (Fig. 3).[53] The outer Helmholtz plane (OHP) represents the closest approach of hydrated ions to the surface, while the inner Helmholtz plane (IHP) is formed by the ions that are chemically adsorbed onto the surface of the electrode.

Many studies have reported effects of the electrolyte's cation(s) on the ECO_2RR in aqueous media. One illustrative example is observed by substituting Li^+ with Cs^+, where the latter cationic species leads to a substantial enhancement of the ethylene selectivity during the ECO_2RR on Cu(100)- and Cu(111)-oriented thin films.[54] Such a cationic effect is mainly related to the tendency of cations to chemically or physically adsorb on the electrode surface, which is governed by the reaction energetics and hydration shell of the cations.[55] The hydration capacity is stronger for smaller alkali cations, with the Li^+ ion binding the water molecules more strongly and being less likely to adsorb on the cathode surface. Conversely, bigger cations are more likely to adsorb onto the electrode surface, shifting the position of the OHL[55] and leading to a lower concentration of H^+ in the vicinity of the active surface that translates into reduced selectivity towards hydrogenated CO_2RR products, such as CH_4.[55] We encourage those readers interested in a more detailed discussion of the effect of the EDL structure on the ECO_2RR to revisit the following literature.[56–58]

3 Electrocatalyst design

Electrocatalysts are essential for the ECO_2RR, since they speed up the rate of this highly complex and kinetically demanding electrochemical reaction. These electrocatalysts hold the potential to substantially improve and modulate the selectivity and kinetics of electrochemical CO_2 reduction, all the while preserving their intrinsic properties. The urgent need to address climate change and reduce anthropogenic CO_2 has pointed out the key role of electrocatalyst design for the ECO_2RR in the coming years.

In the 80s and 90s, ECO_2RR electrocatalysts were classified into different groups according to the metal phase and resulting product selectivity.[59] However, it is currently known that activity and selectivity do not only depend on the nature of the metal phase, but also on complementary properties such as the electronic configuration, catalyst support, surface chemistry, morphology or electric conductivity.[59–62] It is proven that tuning the electronic properties, composition and morphology of the electrocatalysts can significantly modify the density and turnover frequency of the sites/phases active for the ECO_2RR.

Thus, in this section we present and discuss recent developments in ECO_2RR electrocatalysts based on their initial composition, to then delve into the influence of different electronic and structural properties that can tune the ECO_2RR performance, with especial emphasis on electrochemical CO_2-to-CH_4 conversion. To provide a quick overview for the readers, we summarize in Table 2 the most active catalysts reported to date, highlighting key electrochemical parameters.

3.1 Metal electrocatalysts

A simple but vague classification can be made by considering the nature of the metallic phase for bulk materials.[47] Generally speaking, most of the transition metals electrocatalyze the HER more easily than the ECO_2RR in aqueous media, rendering them useless for practical application when seeking CH_4 formation. This HER-selective material group includes Ti and Pt, among others. Complementarily, some transition metals exhibit higher ECO_2RR *vs.* HER performance with preferred selectivity towards CO formation, as is the case of Au, Ag and Zn, or preference towards HCOOH formation, as is the case of In, Sn and Cd. In a more particular scenario, Cu-based electrocatalysts have arisen as the only category capable of converting CO_2 into hydrocarbons, including our target product, CH_4.[59]

Bulk electrodes in the form of metal foils normally require high overpotentials to catalyze CO_2 conversion, and thus many studies have recently focused their efforts on nanostructured materials with a higher ratio of surface-accessible active sites. Moreover, nanostructured materials can exhibit rough surfaces, combinations of oxidation states, small crystalline features and defects that can enhance their ECO_2RR performance with regard to the corresponding bulk transition metal. In the following subsection, we tackle the effect of structural, chemical and electric properties that result in high selectivity towards CH_4 formation.

3.1.1. Cu-based electrocatalysts. As mentioned before, copper (Cu) stands out among other metals due to its capability for converting CO_2 into hydrocarbons, including CH_4, C_2H_4 and C_2H_6, with low selectivity towards a single product.[63] However, understanding the factors that determine this catalytic activity remains a challenge. Modelling works grouped all Cu crystal facets in the order of their ECO_2RR activity, Cu(211) being the most active surface, followed by Cu(110), Cu(100), and finally Cu(111).[64] The findings indicate that Cu(211) is the surface of pure Cu that exhibits the best electrocatalytic activity for both CO and CH_4 formation, which unfortunately makes them non-selective towards the formation of one unique product.

Table 2 Summary of representative electrocatalysts for electrochemical CO_2-to-CH_4 conversion, including their reported active sites, maximum CH_4 faradaic efficiency (FE), operating current density, applied potentials, stability metrics (if reported), and corresponding references. Current densities marked with * refer to partial CH_4 current densities. ** refers to applied voltage instead of applied potential

Active site	CH_4 FE/%	j/mA cm^{-2}	E/V *vs.* RHE	Stability	Electrolyzer	Reference
Cu nanoparticles	76	11	−1.35	—	H-type cell	71
Cu nanoparticles	58	105	−1.00	—	Flow cell	87
Cu nanoparticles	73	234	−1.10	—	Flow cell	88
Cu nanoparticles	60	230	4 V**	50 h	Zero-gap cell	88
CuN_4	55	35	−1.25	12 h	H-type cell	93
CuN_2B_2	73	292	−1.46	8 h	Flow cell	95
CuN_2O_2	78	40	−1.44	6 h	H-type cell	97
La_5Cu_{95}	65	300	−1.72	—	Flow cell	99
Pd single atoms on Cu	60	118*	−1.10	—	Flow cell	103
N_xC-encapsulated Ag nanoparticles	44	7	−1.40	10 h	H-type cell	108
N-doped carbons	15	30	−0.90	—	H-type cell	133
F- and N-doped carbons	99	0.2	−0.80	—	H-type cell	150
Cu single atoms	62	136	4 V**	110 h	Zero-gap cell	171
Cu single atoms	82	400	−0.90	5 h	Flow cell	201

Experimentally, initial studies with Cu foils[65] demonstrated that the preparation conditions of the Cu surface affect selectivity and efficiency towards certain products. The experiments showed that methane is produced when the Cu surface is cleaned with HCl rather than HNO_3 or oxidized in air, suggesting that the oxidation state of Cu significantly influences the reaction mechanisms. Some years later, a few studies demonstrated that improved hydrocarbon selectivity was observed in oxidized Cu foils due to the presence of Cu_2O sites, which act as a more active phase for certain hydrocarbons than metallic Cu.[66–68] More precisely, the work of Mistry *et al.*[66] demonstrated that a H_2 plasma treatment of polycrystalline Cu led to a metallic Cu surface that yielded a large C_1 product selectivity, with a FE for CH_4 formation of 37%. In contrast, an O_2 plasma treatment of polycrystalline Cu produced an oxidized surface with nearly 0% C_1 product selectivity, but a high conversion to C_2 products, including a FE for C_2H_4 of 60%.

Recently, it was demonstrated that the presence of an oxidizing agent in the electrolyte can also modulate the ECO_2RR activity of Cu electrocatalysts. As shown in the literature,[70] oxygen-containing species not only enhance the rate of the ECO_2RR, but also tune selectivity for certain products. The presence of H_2O_2 accelerates the rate of CH_4 production by a factor of 200 in Cu electrodes, whereas in O_2-containing solutions a strong decrease of CH_4 production is observed. The authors relate such behavior to an increase in the surface concentration of oxygen-containing Cu species that, when stabilized, can significantly enhance the ECO_2RR activity and selectivity of such electrodes, in a very similar way to what was discussed above for pre-oxidized Cu samples. In addition, the same authors claimed that selectivity for different products can be tuned by the chemical structure of the oxygen-containing species.

3.1.1.1 Cu nanoparticle electrocatalysts. With advances in nanoparticle synthesis, controlling the size, composition, structure and morphology of Cu nanoparticles is nowadays possible. For such nanoparticulate materials, there are three main parameters that determine the ECO_2RR performance: their composition, size and support. The size of Cu nanoparticles has proven to play a key role in ECO_2RR catalysis. Cu nanoparticles showed high selectivity towards CH_4 formation (FE of 76%), which is substantially superior to the CH_4 FE of polycrystalline Cu (44%).[71] Nevertheless, Cu nanoparticles with a diameter below 15 nm tend to enhance competitive reactions, such as H_2-evolution and electrochemical CO_2-to-CO conversion, significantly lowering the FE towards CH_4.[69] A controlled synthesis of Cu nanoparticles of different sizes is illustrated in the AFM images in Fig. 4A–F. As shown in Fig. 4G and H, the smaller the nanoparticle diameter, the higher the current density in linear sweep voltammetry curves. This enhanced current density is associated with not only an improvement of the ECO_2RR performance, but also an increase in the HER activity. Smaller nanoparticles exhibit a substantial enhancement in selectivity towards H_2, whereas larger nanoparticles tend to favor ECO_2RR products.[69] As a result, large nanoparticle sizes are recommended for hydrocarbon production (Fig. 4I).

Another essential aspect when designing Cu-based electrocatalysts is the catalytic support. The main goal of this support is to inhibit nanoparticle agglomeration during catalyst synthesis and under working conditions,[72] and to provide diffusion channels for the supply of the reactant and the evacuation of the products.[63] Moreover, catalytic supports are also essential to assure electrical conduction paths to the metal sites. The most common supports are based on carbon materials,[73] although other materials can also act as effective supports, such as polymers,[74–76] CeO_2 (ref. 77 and 78) or molybdenum-based 2D materials.[79–81]

Carbonaceous materials are low-cost and abundant catalytic supports, making them promising for reducing electrocatalyst costs.[28] Anchoring metals on carbon materials has been an excellent approach for large-scale electrocatalyst production.[82] The metal phase provides active sites for the ECO_2RR, while the carbon provides a high surface area that reduces diffusion limitations and exposes a higher number of Cu active sites, while ensuring that the metal-support assembly remains electrically conductive.[28] Carbon materials, especially those that are doped with heteroatoms, feature excellent nanoparticle-anchoring capabilities owing to their metal–heteroatom chemical bonds. Nitrogen (N) is by far the most studied heteroatom,[69,83–85] since its similar size to carbon and unique electronic configuration generate electron delocalization in the carbon layers, resulting in an n-type-like semiconductor, as the substitution of a carbon atom with nitrogen introduces an extra electron into the carbon structure, which can move through the electron cloud, enhancing electrical conductivity. Additionally, N atoms strongly interact with metal phases, avoiding nanoparticle leaching and agglomeration and thus enhancing the electrocatalyst's *operando* stability.[86]

One example of such an N heteroatom effect was observed by Dai *et al.*,[87] who anchored Cu on a carbon support through strong metal–heteroatom interaction using pyridine-based N-functionalities (pyridine-substituted graphdiyne (Py-GDY)) obtained by cross-coupling of 1,3,5-triethynyl-2,4,6-tris(4-pyridyl) benzene. The non-doped homologous material (GDY) exhibited larger and more heterogenous Cu-nanoparticle sizes, and while the catalyst prepared with Py-GDY showed excellent ECO_2RR selectivity with a CH_4 FE of 58% at a current density of 105 mA cm^{-2}, the catalyst made with non-doped GDY had a methane faradaic efficiency of only 37% at the same current. The authors attributed this enhanced selectivity for CH_4 formation to the pyridyl groups, which led to strong metal–N interaction that resulted in uniformly dispersed Cu nanoclusters of about 2 nm.[87] In a similar study,[88] the authors prepared Cu nanoparticles supported on an N-doped carbon material that featured excellent properties towards CH_4 selectivity, with a maximum FE of 73% and a CH_4-specific current density of 230 mA cm^{-2} at -1.1 V *vs.* RHE, which is again much higher than that of the analogous catalyst prepared on a non-doped support at the same potential (CH_4-specific current density and FE below 50 mA cm^{-2} and 20%, respectively). In this case, the high methane selectivity was attributed to the pyrrolic N in the vicinity of the Cu nanoparticles, which accelerates the hydrogenation of reaction intermediates.

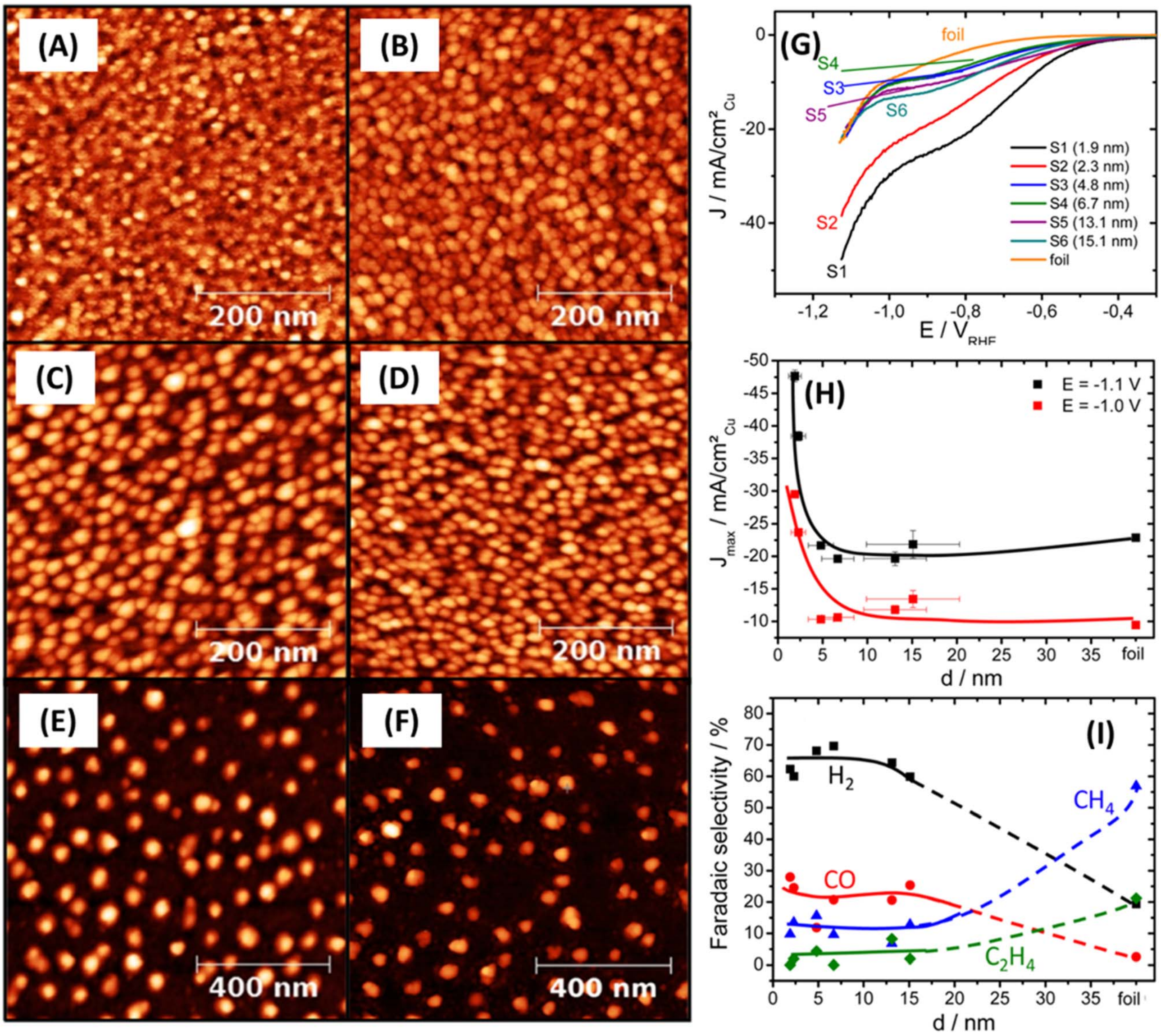

Fig. 4 Tapping-mode atomic force microscopy images of Cu nanoparticles supported on SiO_2 (4 nm)/Si(111): (A) S1, (B) S2, (C) S3, (D) S4, (E) S5, and (F) S6. (G) Linear sweep voltammograms recorded on glassy carbon supports, S1–S6, in a CO_2-saturated 0.1 M $KHCO_3$ solution acquired at room temperature and at a scan rate of 5 mV s^{-1}. Current densities were normalized by the Cu particle surface area after subtraction of the glassy carbon background signal at −1.1 V *vs.* RHE. A Cu foil is included as a reference. (H) Particle size effect during catalytic CO_2 reduction. The faradaic current densities at − 1.1 and −1.0 V *vs.* RHE are plotted against the size of the Cu nanoparticles. The current densities have been normalized by the Cu particle surface area after subtraction of the glassy carbon background signal. (I) Particle size dependence of faradaic selectivity towards various reaction products during the CO_2 reduction reaction. Reproduced from ref. 69 with permission from the American Chemical Society, copyright 2014.

In summary, the surface functional groups in carbon supports have proven to be capable of modulating the selectivity and activity of electrochemical CO_2 reduction towards CH_4 conversion, and thus such functionalities may play a decisive role in the future development of highly effective electrocatalysts for this reaction.

3.1.1.2 Cu single-atom electrocatalysts. The maximized atomic utilization and well-defined coordination of single atom sites make them the most promising active centers among Cu-based ECO_2RR electrocatalysts.[89] The rational design of the coordination of the metal center, including the nature and number of the coordination atoms, affects substantially the electronic structure of the metal site and should cause significant changes in the reaction pathway and product selectivity with regard to the extended metal surface. A Cu–N_4 coordination is the most desirable configuration for the ECO_2RR due to its high stability, stemming from its optimal thermodynamic interaction between Cu atoms and reaction intermediates.[89] It is widely acknowledged that Cu single atoms often produce hydrocarbons with only one carbon atom (*i.e.*, C_1 products) because the lack of adjacent active sites restrains C–C coupling. Beyond this general observation, some studies reported high selectivity towards CH_3OH or CH_4, while a few other studies reported a preference for CO formation.[90,91] The reasons for this discrepancy remain unanswered, with new studies focusing more on electrocatalytic results rather than on understanding these disparities.

As an example, Cu single atoms displaying the above $Cu–N_4$ configuration and incorporated into carbon nanofibers electrochemically reduced CO_2 to CH_3OH with a FE of 44% at a current density of 93 mA cm^{-2}.[92] DFT modelling showed that these $Cu–N_4$ single atoms possess a high adsorption energy for the *CO intermediate[92] and that the free energy barrier of the subsequent *CHO to *CHOH step is much lower than that of the *CHO to $*CH_2O$ path, thus favoring methanol over CH_4 or CO production. However, in a different study, CuN_4 single atoms obtained from Cu phthalocyanine exhibited a high FE towards CH_4 (55% at a current density of – 35 mA cm^{-2}).[93] At the same time, a high CO_2-to-CO conversion was recently reported with CuN_4 single atoms anchored on carbon materials[94] that showed a FE towards CO of > 90%. These are just a few examples of the large variety of selectivity trends reported for CuN_4 sites, for which the disparities remain elusive. All these previous studies have employed DFT calculations to support the reported selectivity and mechanisms, in principle proving the thermodynamic viability of the individual ECO_2RR pathway towards CH_3OH, CH_4 or CO, but without modelling all other possible reaction mechanisms, which make these results inconclusive.

Another important factor that may account for these discrepancies is the nature of the supporting matrix. Beyond simply stabilizing the $Cu–N_4$ moieties, the substrate can strongly influence charge distribution, binding energies of intermediates, and even site stability. For instance, CuN_4 decorated on N-doped carbon dots has been reported to deliver FEs above 80% for ethanol,[95] while Cu single atoms embedded in a porphyrin-based MOF produced CH_4 with a FE of ≈80%.[96] However, the substrate is clearly not the sole determinant: another study on Cu single atoms in a porphyrin-based MOF instead showed a high selectivity towards acetate (>40%) with negligible CH_4 production.[97] These contrasting examples highlight that the catalytic outcome arises from a complex interplay between the atomic site and the physicochemical properties of the support and that decoupling these contributions remains a major challenge. It should also be emphasized here that many metal-free catalysts, especially carbon-based materials, are catalytically active for the ECO_2RR (see Section 3.2 Metal-free carbon-based electrocatalysts), which further complicates the interpretation of activity trends.

A potential strategy to address the discrepancies is the application of advanced *in situ*/*operando* spectroscopic techniques capable of resolving reaction intermediates under realistic electrochemical conditions. We believe that by directly tracking adsorbed species and identifying the rate-determining steps, the field can move beyond purely thermodynamic DFT predictions, which often neglect alternative pathways and dynamic effects under operating conditions. At the same time, the current understanding of the role of the supporting material remains limited. In this regard, *in situ*/*operando* characterization will be essential not only to determine the intrinsic activity of CuN_4 sites, but also to understand why their catalytic properties vary so markedly depending on other factors such as the local coordination environment, the supporting material, and the surrounding reaction microenvironment.

Nevertheless, given the current lack of mechanistic consensus, many studies have adopted an empirical approach by tuning the local environment of the SAC's metal centers to directly modulate ECO_2RR selectivity. The introduction of B atoms into the local coordination of the Cu single atoms, especially in the $Cu–N_2B_2$ configuration, results in a significant increase of the catalyst's selectivity towards CH_4 formation, with a FE of 73% at a partial current density of −292 mA cm^{-2},[98] as opposed to only 30% CH_4 at barely 100 mA cm^{-2} at the same potential (-1.46 V *vs.* RHE) for the analogous $Cu–N_4$-based material. The authors attribute this improvement brought about by the introduction of B to a lower energy requirement for the *CO to *CHO thermodynamic barrier.

Interestingly, similar effects were found when introducing a low concentration (5% on a catalyst weight basis) of Cu single atoms in CeO_2 nanorods. Such an addition induced a substantial increase in the CH_4 selectivity up to a FE of 58% due to the creation of oxygen vacancies surrounding the $Cu–N_4$ sites.[99] Similarly, the introduction of oxygen atoms coordinated directly to the Cu single atoms (*i.e.* in the form of CuN_2O_2) can also efficiently modify the electronic structure of the metal center for reducing the thermodynamic barriers towards CH_4 formation.[100] As a result, the CuN_2O_2-containing electrocatalysts show a superior CH_4 selectivity with a FE of 78% at −1.44 V with a total current density of 40 mA cm^{-2}.

In summary, the modulation of chemistry in the local coordination or vicinity of $Cu–N_4$ sites seems to be a promising strategy to reach high selectivities towards CH_4 formation. Further studies with different heteroatoms, defect engineering and pioneering synthesis strategies are mandatory to obtain even more selective materials and a better understanding of the mechanisms behind these phenomena.

3.1.1.3 Cu-based bimetallic electrocatalysts. The electrocatalytic activity of CO_2-to-CH_4 electrochemical conversion appears to be related to the linear relationship between the adsorption energies of *CO and *CHO intermediates, which restricts selectivity towards CH_4 formation. The inclusion of a second metal either in the form of a single atom (using the so-called dual-site configuration) or through the alloying of metallic Cu with a second element can provide a new degree of freedom to modulate this adsorption energy difference, allowing better selectivity towards CH_4.[101]

Dual Cu adjacent sites have also been proposed as a promising pathway to increase selectivity towards hydrocarbon products.[89,103] Although this system is not strictly a bimetallic material, we find it useful to include it in this section because the results of adding an additional Cu atom closely resemble those observed in bimetallic materials rather than in single-atom Cu catalysts. In dual-site Cu catalysts, two neighboring Cu atoms are anchored onto a support and work cooperatively to enhance CO_2 reduction activity. In these systems, Cu atoms serve as active sites for $*CO_2$ adsorption and when two $*CO_2$ intermediates are adsorbed close to each other, the proximity significantly favors C–C coupling reactions, leading to the formation of hydrocarbons, especially C_{2+} products.[103] Such a synergistic effect of dual Cu sites was further demonstrated through the tuning of the distance between neighboring Cu sites, which modulated selectivity to different hydrocarbons, allowing the formation of C_{2+} products. At Cu concentrations above 4.9 mol%, the distance between adjacent CuN_4 species was close enough to enable C–C coupling of ECO_2RR intermediates, resulting in high selectivity towards C_2H_4.[104] In contrast, concentrations below 2.4 mol% demonstrated high selectivity towards CH_4.[104] Thus, the metal content and corresponding distance between CuN_4 sites are of high relevance for product selectivity.

In the case of bimetallic alloys, a large number of studies have tried to overcome the low selectivity of Cu-based electrocatalysts for the formation of CH_4 through the synthesis of Cu-based bimetallic alloys. More precisely, trace amounts (from 0 to 7 at%) of oxophilic metals (La, Pr, Y, and Sm) were introduced into a pure Cu matrix for evaluating ECO_2RR performance.[102] As observed in Fig. 5A, DFT calculations showed that the oxophilicity of the alloying metal correlates strongly with the adsorption energy of *CHO, which is known to be a key parameter for ECO_2RR selectivity. Experimentally, the introduction of La into the Cu structure in a La_5Cu_{95} ratio resulted in an excellent partial current density of 194 mA cm^{-2} (Fig. 5B) with a high FE towards CH_4 of 64.5% at 300 mA cm^{-2} (Fig. 5C). This is attributed to the alloying of Cu with La, which not only stabilizes the *CHO intermediates, but also promotes the splitting of the C–O bond in the *CH_3O reaction intermediate by forming a stable La–O bond (Fig. 5D). Similar conclusions were found through the introduction of Bi into a Cu aerogel,[105] which resulted in the variation of the Cu^{2+}/Cu^{+} ratio on the electrocatalyst surface and in turn led to different FEs towards ECO_2RR products (Fig. 6A). In particular, the highest FE towards CH_4 was obtained for a $Cu_{50}Bi$ material that displayed a FE towards CH_4 of 26% at a total current density of 150 mA cm^{-2}. Additionally, as observed in Fig. 6B, the tuning of the Cu_XBi composition leads to a significant modification of the ECO_2RR selectivity, with FEs towards CO above 80% in the case of $Cu_{100}Bi$, or 60% FE towards formate with Cu_5Bi. Interestingly, the higher Cu^{2+}/Cu^{+} ratio increased significantly the selectivity for CH_4 formation, hypothetically due to favoring of the hydrogenation of reaction intermediates.

Another interesting study tried to integrate H-affine elements within Cu. Although platinum-group elements are known for their high HER-selectivity, when atomically

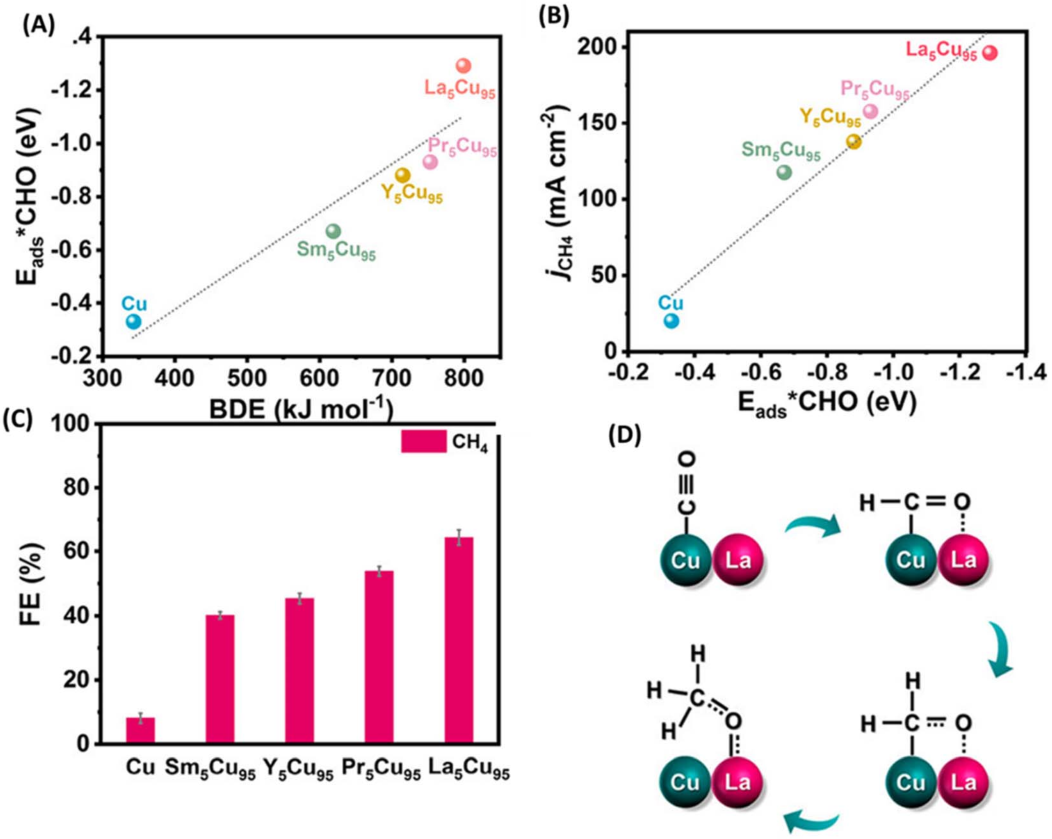

Fig. 5 (A) Relationship between calculated *CHO adsorption energy (energy required to convert one molecule from the lowest adsorbed state to the lowest gaseous state) and the bond dissociation enthalpy (BDE) of the metal–oxygen bond. (B) Relationship between the partial current density of CH_4 at a total current density of 300 mA cm^{-2} (in CO_2-saturated 1 M KOH solution) and the adsorption energy of *CHO for Cu and M_5Cu_{95} electrocatalysts. (C) FE of CH_4 on Cu and M_5Cu_{95} electrocatalysts at a total current of 300 mA cm^{-2}. (D) Proposed reaction pathways of the ECO_2RR to CH_4 on the La_5Cu_{95} surface. Reproduced from ref. 102 with permission from the American Chemical Society, copyright 2023.

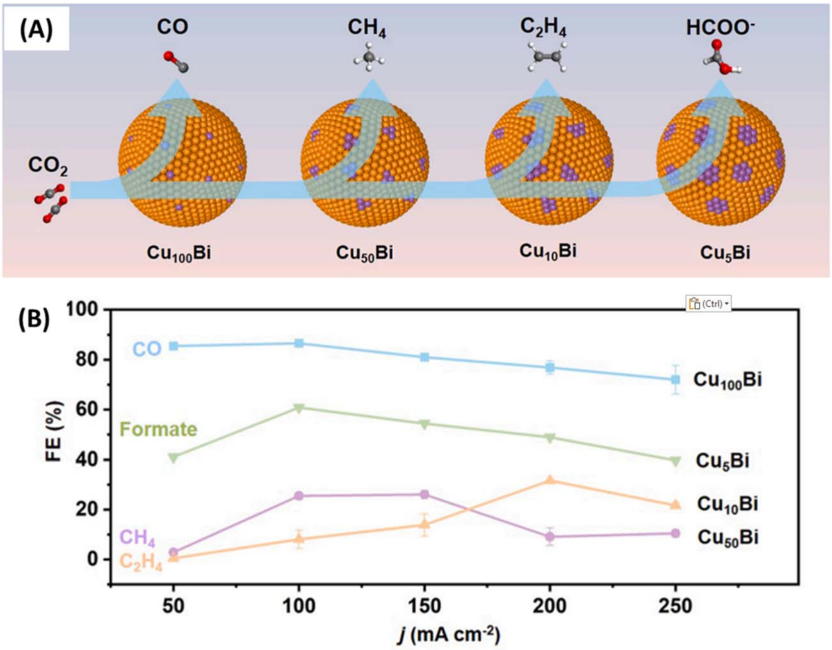

Fig. 6 (A) Product distribution of the ECO_2RR with different Cu_XBi compositions. (B) Electrocatalytic performance (in CO_2-saturated 1 M KOH solution) of the corresponding Cu_XBi aerogels, showcasing the FEs for ECO_2RR products at different applied current densities for $Cu_{100}Bi$, $Cu_{50}Bi$, $Cu_{10}Bi$ and Cu_5Bi. Reproduced from ref. 105 with permission from Elsevier, copyright 2022.

dispersed platinum atoms are integrated into a shape-controlled Cu catalyst, they increase the selectivity towards hydrocarbon products. For instance, Pt-group single atoms act as H* donors and facilitate the hydrogenation of *CO intermediates in polycrystalline Cu surfaces.[106] The incorporation of Pd single atoms into Cu-based electrocatalysts led to an increase in the CH_4 partial current density from 2.3 to 118 mA cm^{-2} (Fig. 7A), with an improvement of FE towards CH_4 from 2 to 60% at −1.1 V *vs.* RHE (Fig. 7B). Moreover, the alloy phase morphology is also relevant, since spherical or cubic structures resulted in high C_{2+} yields, whereas octahedral structures promoted CH_4 formation (Fig. 7C). Chiefly, this strategy of adjusting the metal nature and metal doping to tune the *CHO adsorption energy can be extended to increase the hydrocarbon selectivity of Cu electrocatalysts towards products other than CH_4.[107,108]

3.1.2. Silver-based electrocatalysts. Ag-based electrocatalysts are of the greatest interest for CO production because of this metal's relatively low cost (particularly when compared with noble metals) and high selectivity for this product.[109] This is why most of the studies that focus on Ag electrocatalysts for the ECO_2RR do so with a strong focus on CO production. However, the size, crystal structure and morphology of silver (nano)catalysts can further tune their ECO_2RR performance. As a result, Ag-based electrocatalysts in which the properties of the pristine metal have been tuned through the addition of a second metal phase have recently emerged as a promising approach for the electrochemical conversion of CO_2 into CH_4.

As an example of this, a 2017 study showed that Ag–Co bimetallic electrocatalysts with electronic properties different from those of the monometallic Ag counterpart featured a methane FE of 20% at an applied voltage of 2.0 V (*vs.* nearly 0% for the monometallic catalyst) thanks to the atomic rearrangement and concomitant tuning of the binding strength of the *CO intermediate, which favors CH_4.[110] Specifically, Co atoms provide free electrons to the vacant orbitals in Ag, forming Ag–Co bonds that induce large changes in the electron density of the metals and shift ECO_2RR selectivity towards CH_4 instead of CO. Similarly, the deposition of a N_xC shell surrounding the Ag nanoparticles also serves to tune product selectivity,[111] in this case not through a modification of silver's electronic properties, but by prolonging the residence time of the *CO intermediate on the catalyst's surface and increasing the number of hydrogenation reactions. As a result, the FE for CH_4 formation was enhanced above 44% after the creation of the N_xC nanoshell, as compared to nearly 0% in the absence of the latter (*i.e.*, for bare Ag nanoparticles).

In summary, although there are not many studies that focus on modifying the ECO_2RR selectivity of Ag electrocatalysts, the few studies discussed above demonstrate that tuning silver's properties can also be a promising strategy towards CH_4 formation.

3.1.3. Cobalt-based electrocatalysts. DFT computations indicate that the chemisorption of the *CO_2 intermediate is the rate-limiting step for the ECO_2RR on CoN_4 sites.[112] While CO is the main product for such Co-based electrocatalysts,[113] CH_4 is eventually produced in minor amounts due to the hydrogenation of the *CO intermediate. This is confirmed experimentally, since a FE towards CO of 97–99% was obtained when investigating Co phthalocyanine as the ECO_2RR active site, and

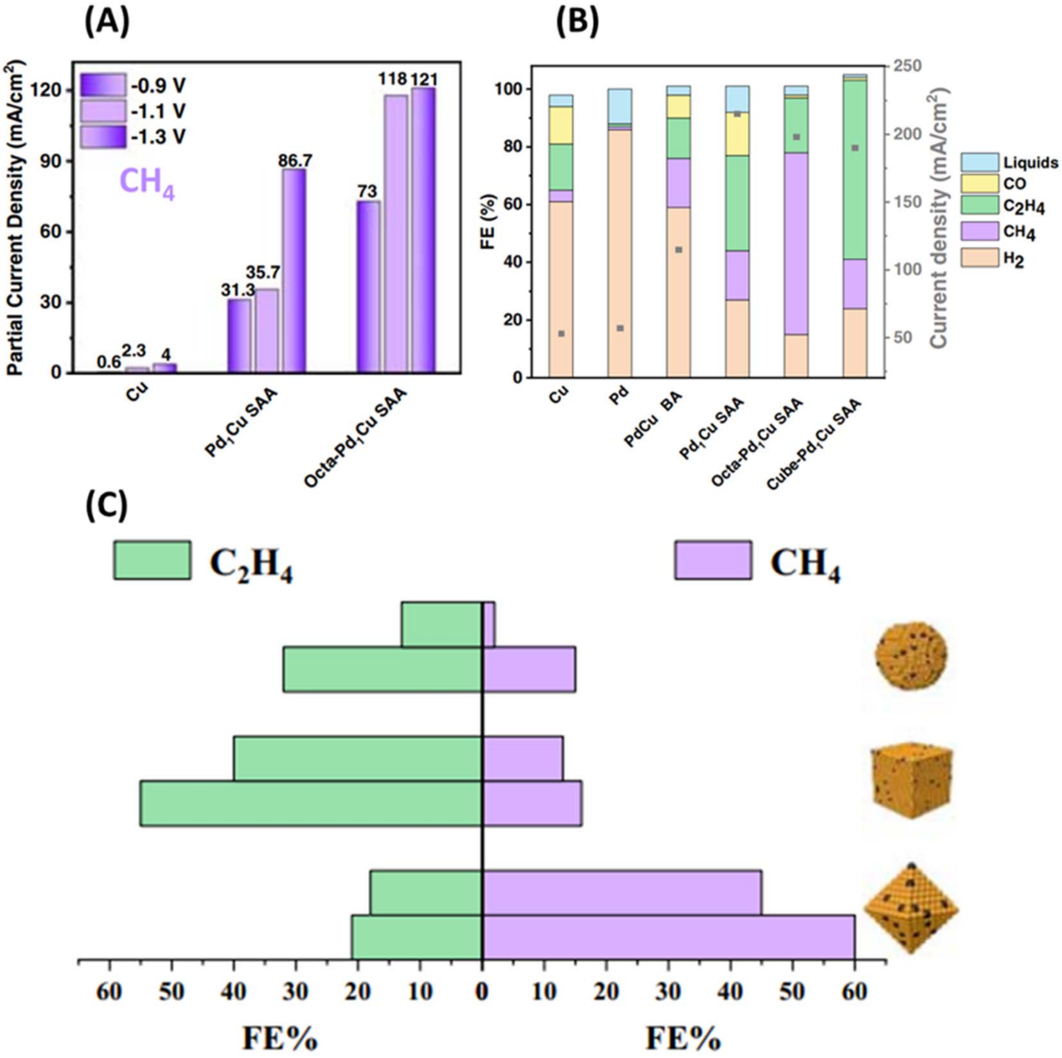

Fig. 7 (A) Partial current density for CH_4 at different voltages for polycrystalline Cu, polycrystalline Pd_1Cu configuration and shape-controlled Octa-Pd_1Cu configuration. SAA stands for single-atom alloys. (B) Comparison of CO_2 reduction FE (%) and current densities of Pd_1Cu configuration and analogues. The FE was obtained from amperometric *i*·*t* curves at −1.1 V *vs.* RHE (in a CO_2-saturated 0.5 M $KHCO_3$ solution) and quantifying the products over 30 min. (C) FE distribution of CH_4 and C_2H_4 obtained using Cu and shape controlled Pd_1Cu materials. Reproduced from ref. 106 with permission from Springer Nature, copyright 2023.

negligible formation of CH_4 was observed.[76,114] Nevertheless, even if the majority of Co-based ECO_2RR electrocatalysts are designed for CO production, strategies again exist to improve their selectivity towards CH_4.

For instance, electrochemical CO_2-to-CH_4 conversion has been achieved when employing photo-assisted electrochemical methods.[115] The addition of light illumination during electrocatalysis promotes the stabilization of the *CO intermediate adsorbed on the Co–N_4 sites, allowing its subsequent hydrogenation to yield CH_4. Along these lines, the incorporation of Co phthalocyanine into Zn–N–C materials caused a 100-fold enhancement in the selectivity of the latter materials towards CH_4 formation.[116] DFT calculations revealed that the first reduction of CO_2 molecules occurs at the Co–N_4 sites, but the resulting *CO intermediate is transferred onto the Zn–N_4 sites for further conversion into CH_4.[116]

Interestingly, a strong effect of the supporting electrolyte was also observed in Co porphyrins.[117] Cation size affects the reaction in two ways: large cations, such as K^+, enhance the HER because smaller cations retain more water, creating steric hindrance that slows H^+ diffusion. Conversely, small cations, such as Li^+, stabilize the key intermediate of CO_2 reduction through ion pairing, facilitating the conversion of CO_2 into CO and CH_4.[117]

3.1.4. Fe-based electrocatalysts. Fe is among the most promising transition metals for catalyzing many electrochemical reactions due to its high abundance and corresponding low cost.[118–121] This means that tuning the electronic properties of Fe electrocatalysts is not a new strategy in materials science, but how this approach affects these materials' ECO_2RR performance is still unknown. Furthermore, the poor HER activity of Fe-based electrocatalysts (typically requiring overpotentials > 400 mV (ref. 82)) underscores the capabilities of these electrocatalysts for promoting CO_2 electroreduction over H_2 production.

Iron, especially in the form of single atoms with an FeN_4 coordination, is known to electrochemically reduce CO_2 to CO with high selectivity (*i.e.*, a FE > 90%).[122–124] The correspondingly poor selectivity towards CH_4 formation is mainly associated with the isolated nature of the FeN_4 active sites. Computations indicate that the ECO_2RR in FeN_4 sites can indeed proceed beyond CO.[125] Specifically, since FeN_4 sites are excellent CO producers and therefore can form a large amount of *CO intermediates, these reaction intermediates can be further reduced until yielding hydrocarbons. However, this work suggested that highly active CH_4 formation may require an extended surface or nearby proton source to lower the protonation barrier.[125]

We are only aware of one study in which Fe exhibited CH_4 formation.[126] This work explored structure–activity relations in FeN_4 catalysts, revealing that the catalytic activity is strongly influenced by the nitrogen functionalities. Specifically, XPS data suggested that pyridinic N and FeN_4 moieties serve as active sites, as they promote CO_2 adsorption and facilitate electron transfer. *Operando* EXAFS results indicated a change in the Fe oxidation state from Fe^{2+} to Fe^{1+} at potentials of approximately −0.9 to −1.1 V *vs.* RHE, coinciding with the onset of CH_4 production. The authors attributed this CH_4 formation to the FeN_4 sites with the Fe atom in the +1 oxidation state. While CH_4 production remained very low (<1%), this redox transition offers a potential pathway to enhance the CO_2-to-CH_4 activity of FeN_4 sites by tuning their electronic configuration.

3.2 Metal-free carbon-based electrocatalysts

In the pursuit of low-cost ECO_2RR electrocatalysts, metal-free carbon-based materials have emerged as an excellent alternative to those containing metals.[28,127,128] Nevertheless, even if these metal-free electrocatalysts have been extensively proven to be effective for other electrochemical reactions such as oxygen reduction[129,130] and hydrogen evolution,[130,131] their ECO_2RR performance is still far from that of metal-containing materials. Pristine, undoped carbon materials exhibit minimal catalytic activity towards the ECO_2RR because the electron density across their carbon layers is homogenously distributed.[132] A common strategy to improve this poor catalytic performance involves altering and tuning their electronic properties through the introduction of heteroatoms, surface functionalities, and defect engineering and curvature. Incorporating functional groups or defects into the basal plane of the carbon layers usually induces a redistribution of electron density through electron withdrawal-donation effects that localize the charge in carbon atoms adjacent to defects or heteroatoms. This electron delocalization near heteroatoms tends to attract the reagent molecule more easily, and when the molecule is chemically adsorbed at the active sites, the polarization of the carbon electrode induces its subsequent reduction.

Nitrogen is the most commonly studied heteroatom when it comes to doping carbon materials due to its similar size to carbon, but also because of its larger electronegativity (3.04 for N and 2.55 for C). N-doped carbon materials have proven to be effective electrocatalysts for multiple electrochemical reactions, including the ECO_2RR. Nitrogen atoms can be incorporated into carbon materials in the form of different functionalities that can be classified according to their binding energies:[133–135] pyridinic-N (398.4 eV), pyrrolic/pyridonic-N (400.3 eV), graphitic-N (also called quaternary-N, 401.2 eV) and oxidized-N (402.9 eV). In general, the defects located at the edge of the carbon layers are assumed to be more active than those at the basal plane, with N-doped zigzag species being the most active site among these.[136] Fig. 8a shows HRTEM images of N-doped graphene quantum dots (NGQDs) 1–3 nm in size that were prepared through exfoliating and cutting graphene oxide with *in situ* N doping. The N 1s XPS spectrum confirmed the N doping in the form of pyridinic, pyrrolic and graphitic N species (Fig. 8B). Pristine non-doped GQDs showed indeed moderate ECO_2RR activity thanks to their large edge density, with a current density of around 10 mA cm^{-2} at −0.85 V *vs.* RHE and high selectivity towards CO (FE = 10%) and $HCOO^-$ (FE = 6%).[137] However, the high N content at the basal plane of NGQDs resulted in a significant improvement of the catalytic activity with a current density of 100 mA cm^{-2} at the same potential and enhanced selectivity for CH_4 and C_2H_4 products (Fig. 8C and D).[137] Among such N species, pyridinic functional groups appear to be responsible for variations in the selectivity in metal-free carbon-based electrocatalysts, as this edge-type N species substantially decreases the energy barrier for the formation of the *COOH intermediate, which mainly leads to CO production.[138,139] For high CH_4 or C_{2+} production, N species located in the basal plane, such as graphitic N, appear to be the most promising in terms of selectivity. However, for graphitic N, the extra electron located in the π* antibonding orbital is less accessible for CO_2 chemisorption, as proved by the 1 eV higher chemisorption energy of graphitic N when compared to pyridinic N.[140] Nevertheless, even with this thermodynamic barrier, graphitic N remains better than the N-free, pristine carbon, as demonstrated by its better ECO_2RR activity.[140]

Here it is worth noting that both graphitic and pyridinic N induce an electron withdrawal effect in the adjacent carbon atoms, which leads to a redistribution of the charge density in the carbon matrix.[139–141] This results in a negative electron density in the N atom and a corresponding positive charge density in the first neighbor carbon atoms. These negatively charged sites act as active centers onto which the positively charged C atoms from the CO_2 molecules chemisorb, forming a N–CO_2 intermediate. In the case of pyridines, the chemisorption occurs *via* sp^2-to-sp^3 hybridization, facilitating CO_2 chemisorption. However, graphitic N already forms three chemical bonds with adjacent carbon atoms, making the creation of an additional chemical bond with the CO_2 molecule highly energy demanding. This is why the carbon atoms in the vicinity of the N functionality are considered the active sites in the case of graphitic N groups. However, in modelling graphitic N, C–CO_2 chemisorption is often proposed on the carbon atom located in the *ortho* position,[142] which appears unlikely when considering these C atoms' positive charge

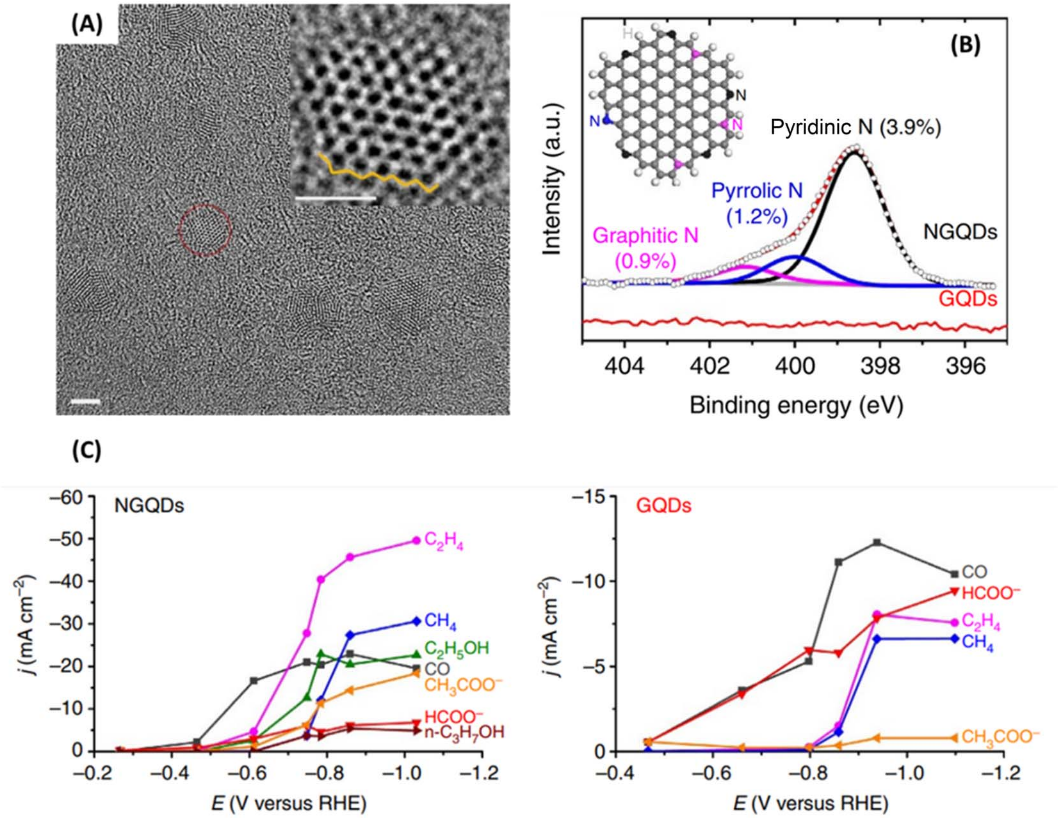

Fig. 8 (A) TEM image of NGQDs (scale bar, 2 nm), with the inset showing a high magnification image of a single NGQD containing zigzag edges outlined by the yellow line (inset scale bar, 1 nm). (B) N 1s XPS spectrum of the NGQD sample, deconvoluted into pyridinic, pyrrolic and graphitic N. The value in parentheses is the corresponding N atomic concentration. (C) Partial current densities as a function of the cathode potential for various electrochemical CO_2 reduction products when using NGQDs (left) and GQDs (right) as the electrocatalysts. Reproduced from ref. 137 with permission from Springer Nature, copyright 2016.

induced by the N functionality. Therefore, it is anticipated that the active sites involve the C atom in the *meta* position to the N through a C–CO_2 interaction or the C atom in the *ortho* position through interaction with the oxygen atoms of the CO_2 molecule through a C–OCO intermediate. As such, further studies are mandatory to unravel the mechanisms behind the ECO_2RR in N-doped carbon materials.

Other heteroatom elements have also been studied as doping agents in carbon materials, such as B,[143–145] F,[146,147] P[148–151] or S.[152,153] Furthermore, heteroatom doping with these elements has also been carried out with the aim of tuning the electronic structure of the carbon layers and inducing larger electron delocalization for further ECO_2RR studies. One particularly interesting article claimed to reach a FE towards CH_4 formation of 99% with an F- and N-codoped carbon material.[154] However, this high selectivity was only reached with a very low current density of 0.2 mA cm^{-2}. Recently, adjacent N and B atoms in N- and B-codoped carbon materials have also demonstrated high CH_4 selectivity (*i.e.*, a FE of 68%) and a current density of ≈15 mA cm^{-2} at −0.5 V *vs.* RHE.[155]

In summary, metal-free heteroatom-doped carbon materials are still at the earliest stage of development as ECO_2RR-electrocatalysts. As observed in Table 2, their overall current density remains far below that of metal-containing electrocatalysts, with the best reported current density reaching 40 mA cm^{-2} so far. This large performance gap raises critical questions regarding their practical scalability. Nevertheless, an intriguing characteristic emerges when comparing both families of catalysts. While metal-containing electrocatalysts require very negative potentials to achieve CH_4 formation, metal-free electrocatalysts can achieve high FE for CH_4 already at moderate potentials between −0.5 and −0.9 V *vs.* RHE. This suggests that, although less active in absolute terms, metal-free catalysts may intrinsically demand lower overpotentials to trigger efficient C–H bond formation. Importantly, long-term stability under operating conditions has not yet been demonstrated for metal-free catalysts, which remains a major barrier for their practical applications. Further advances in catalyst design and mechanistic understanding are therefore mandatory to assess whether such features can be leveraged for scalable and competitive implementation.

4 Electrochemical CO_2 electrolyzers

The ECO_2RR performance is not only influenced by the selection of the electrocatalyst, but also by the design of the electrochemical reactor (commonly referred to as a CO_2 electrolyzer) where CO_2 is converted into a value-added product. From an industrial perspective, one of the most crucial requirements for the practical deployment of CO_2 electrolyzers is their ability to operate at high current densities, typically at least 200 mA cm^{-2}. Achieving such high current densities is essential for ensuring economically viable reaction rates and maximizing CO_2 conversion efficiency at scale. However, maintaining high activity while preserving selectivity and stability poses significant engineering challenges, as it requires optimizing not only the catalyst, but also the overall reactor architecture (including the balance of plant), mass transport properties and ion management.

The geometry of the CO_2 electrolyzer, including the electrode and electrolyte configurations, plays a crucial role in determining the mass transfer efficiency of the gaseous reactant and the reaction products. These factors have a direct impact on key performance metrics, such as electrocatalytic selectivity, long-term stability and overall CO_2 conversion efficiency. While extensive research has been dedicated to the development and optimization of electrocatalysts to enhance CO_2 reduction activity and selectivity, less attention has been paid to the practical implementation of these catalysts in application-relevant CO_2 electrolyzers, and comparatively fewer studies can be found on this important topic.

Before delving into the different types of CO_2 electrolyzers, it is important to highlight the critical role of membranes, which are an essential yet often overlooked component in these systems. Membranes serve multiple key functions, such as enabling ion transport between the electrodes, preventing unwanted product crossover, and maintaining system stability, all of which directly impact the overall efficiency and selectivity of the electrolyzers. Since membranes are an essential component in CO_2 electrolyzers and exist in various types, it is important to first explain their nature and functions to understand their application in different electrolyzer types.

4.1 Ion exchange membrane (IEM) CO_2 electrolyzers

A fundamental component of any CO_2 electrolyzer is the membrane, which acts as a selective barrier that regulates the transport of ions between the electrode compartments while preventing the undesired crossover of reactants and products, which can lead to efficiency losses and reduced selectivity.[156] Depending on their ion transport properties, membranes can be classified into three main types: cation exchange membrane (CEM), anion exchange membrane (AEM) and bipolar membrane (BPM). Each of these membrane types has different characteristics that influence the reaction environment and can significantly influence electrolyte pH, ionic conductivity, and product separation, ultimately affecting the performance and feasibility of the system under industrially relevant conditions.[156]

Beyond their electrochemical role, membranes also have a significant economic impact on the viability of CO_2 electrolyzers. The choice of IEM not only dictates performance metrics but also plays a crucial role in determining operational costs, particularly in large-scale applications. Importantly, these costs are not limited to the intrinsic price of the membrane itself but extend to the entire system configuration that each membrane requires. Certain membranes impose operational constraints that necessitate additional infrastructure or system modifications to compensate for their drawbacks. A holistic approach was developed to assess and optimize the economic factors involved in the electrochemical conversion of CO_2 to CO based on different IEMs.[157] Although that study did not focus on CH_4 production, we believe that it properly illustrates the costs associated with each IEM type for electrochemical CO_2 conversion. Mass and energy balances were computed using state-of-the-art literature data and revealed that 75 to 84% of the total production costs can be attributed to the electrolyzer cost. According to the study,[157] AEMs are expected to be the most suitable membranes for ECO_2RR electrolysis due to the low electricity and capital costs associated with their use, leading to an estimated CO-production cost of $\approx$ 800 € t_{CO}^{-1}. This is closely followed by BPMs, which feature a competitive cost of $\approx$ 840 € t_{CO}^{-1}, and CEMs with a higher cost of $\approx$ 1100 € t_{CO}^{-1}.

Given the importance of the membrane choice in both economic and performance terms, it is essential to delve into the specifics of each IEM type. In the following section, we will analyze the characteristics, advantages and challenges associated with each IEM category, providing a comprehensive understanding of how this influences CO_2 electrolysis systems.

4.1.1. Cation exchange membranes (CEMs). Cation exchange membranes (CEMs) are a class of IEMs that selectively allow the passage of cations, such as H^+ or K^+, while blocking the movement of anions. These membranes are widely used in electrochemical systems, including CO_2 reduction electrolyzers, due to their ability to maintain ionic conductivity and decrease the extent of unwanted crossover of reactants and products.

One of the major challenges of CEMs is the acidic pH at the cathode electrode, which promotes the competitive HER over CO_2 reduction. To mitigate this limitation, CEM-based CO_2 electrolyzers, in particular those with electrolyte fed at the anode compartment, can also be operated with a high concentration of K^+ cations from the electrolyte solution, such as $KHCO_3$ or K_2CO_3. The high concentration of K^+ in the electrolyte leads to the diffusion of K^+ through the membrane, replacing H^+ ions at the cathode, and consequently suppressing HER and improving the selectivity for CO_2 reduction.[158] The resulting pH-buffer effect strongly correlates with the hydration shell of the electrolyte cation, which is in turn associated with its permeability and diffusion coefficients.[159] Considering an inverse relationship between the diffusion coefficient and cation hydration radii, the diffusion coefficient for alkali cations follows the order $Cs^+ > K^+ > Na^+ > Li^+$.[159] This implies that, from a device-operation perspective, maintaining high selectivity towards CO_2 reduction requires precise control over the electrolyte composition and ion concentration. However, as we will explain later in the CO_2 electrolyzers section, this strategy is only useful for CO_2 electrolyzers that employ liquid electrolytes, which introduces several challenges, such as high electrical resistance, limited CO_2 solubility and concomitantly low current densities.

Another critical concern in CEM-based CO_2 electrolysis is the crossover of CO_2 products during operation, which leads to the need for including additional separation and regeneration processes and would increase these devices' operational complexity. Although CO_2 crossover is not a significant issue, CO_2-derived alcohols, such as methanol and ethanol, are more problematic with regard to crossover due to their high diffusion coefficients in CEMs.[160,161]

4.1.2. Anion exchange membranes (AEMs). Anion exchange membranes (AEMs) serve as a key alternative to CEMs in CO_2 electrolyzers, offering the advantage of selectively allowing the migration of anions, such as OH^-, HCO_3^- and CO_3^{2-}, while blocking cations. AEMs are particularly advantageous in CO_2 electrolysis because they create a neutral-to-alkaline environment at the cathode, which promotes the CO_2 reduction reaction over the HER.[162] As for the nature of the anionic species, while OH^- anions are produced from the reduction of H_2O and/or CO_2 in the cathodic catalyst layer, their reaction with CO_2 results in carbonate and bicarbonate anions (with the distribution of these species' concentrations being determined by the local pH), and all three species get transported through the AEM to the anode to yield H_2O, O_2 and CO_2 molecules resulting from the oxidation of HCO_3^- and/or CO_3^{2-}.[163–165] This CO_2 regeneration at the anode decreases the electrolyzer's net carbon dioxide consumption and makes it mandatory to put into place additional separation steps that substantially increase the electrolyzer cost[166] and can be more energy-demanding than the CO_2 electrolyzer itself.[163–165] Indeed, the separation of the CO_2 that has crossed the membrane to the anode compartment is estimated to be ≈ 1.6 times more energy demanding than the ECO_2RR step.[167]

Similar to what was discussed above for CEM-based CO_2 electrolyzers, the crossover of products from the cathode to the anode is a major bottleneck for AEM CO_2-electrolysis development. Indeed, it has been reported that more than 30% of all cathodic liquid products cross the AEM to the anode compartment.[168] This crossover increases linearly with current density and CO_2 flow rate and makes it significantly difficult to obtain high energy efficiencies. However, this product crossover is minimized when the targeted product is not a liquid but a gas, such as CH_4, although crossover of volatile products through the GDE can also occur through evaporation.[168] Nevertheless, the high selectivity and efficiency of AEM-based electrolyzers compared to CEM-based ones nearly compensate for such a substantial extra cost of recycling CO_2 from the anode.[162] This advantage stems from AEM electrolyzers' neutral-to-alkaline operative pHs in the cathode electrode, which mitigate the acidic conditions that facilitate the HER over the CO_2RR in CEM-based devices (*vide supra*).[169] This is also advantageous for the counter reaction in the anode, the oxygen evolution reaction (OER), since CEMs' acidic conditions limit the choice of OER electrocatalytic materials to scarce and expensive Ir oxides, which would jeopardize the system's upscale potential due to their high costs.[170] Instead, such medium-to-high pHs at the anode allow the use of OER electrocatalysts based on non-precious metals such as Co or Ni, which drastically reduces the electrolyzer price.[171–173]

Palladium-based and Cu-based electrocatalysts were tested as cathode electrodes for the ECO_2RR in AEM-based flow cell electrolyzers.[174] The Pd electrocatalysts showed a FE towards CO of 98% with a current density of 200 mA cm^{-2}. Similarly, Cu electrocatalysts were evaluated under the same conditions, with a FE of 82% towards hydrocarbons with a current density of 350 mA cm^{-2}. The electrochemical CO_2-to-CH_4 reduction reaction is, however, less studied in AEM-type electrolyzers. Nevertheless, a few studies have proven that the alkaline pH of AEM-type electrolyzers can also lead to high selectivity towards CH_4 formation, with FEs of 62 to 73%.[88,175]

4.1.3. Bipolar membranes (BPMs). The above limitations regarding product and ion crossover have recently been reported to be reduced through the use of bipolar membranes (BPMs), which in their simplest version consist of an AEM and a CEM laminated against each other.[156,171,176,177] It is worth mentioning that two configurations can be applied when implementing a BPM in a CO_2 electrolyzer. First, in the so-called reverse bias (RB) mode that has become the most common configuration in CO_2 electrolysis, the anion- and cation-exchange layers (AEL and CEL) are disposed at the anode and cathode compartments, respectively (Fig. 9). Moreover, water is split at the CEM–AEM interface, which therefore acts as a H^+ and OH^- donor. The protons obtained from the water splitting are transported through the CEL to the ECO_2RR electrocatalyst and react with the reduced species obtained from the ECO_2RR. On the other side, OH^- anions obtained from the water split at the BPM junction are transported by the AEL to the OER electrocatalysts, where they react with the oxidized species of the anode electrode.

Large current densities have been obtained in the RB-BPM mode. Co phthalocyanine was reported as an excellent electrocatalyst for the ECO_2RR in a RB-BPM-type electrolyzer, reaching a CO FE of 62% at a current density of 200 mA cm^{-2} with aqueous CO_2-saturated 1 M KOH anolyte.[178] The use of KOH as the anode electrolyte produces cation crossover that can damage the electrochemical devices. If KOH is substituted with pure water, the current density is reduced to 100 mA cm^{-2} for a similar FE at the same potential. Ni-based electrocatalysts were also tested in RB-BPM mode, with lower CO selectivity (FE of 30%) with a high current density of 100 mA cm^{-2}.[179] Interestingly, Cu-based electrocatalysts were also evaluated in this configuration,[180] with significant selectivity towards multicarbon products (C_{2+} FE of 25%) at a current density of 100 mA cm^{-2}. At higher current densities, the HER predominates over CO or multicarbon selectivity.

The second configuration of the BPM electrolyzer is the so-called forward bias (FB) mode, in which the CEM is located in the anode and the AEM is in the cathode, thus contrary to the RB-BPM case (see Fig. 9). This approach has gained attention in the last few years due to the suppression of CO_2-crossover drawbacks and the elimination of low pHs in the cathode. Regarding the former, the carbonate and bicarbonate anions generated at the cathode are transported by the BPM's AEM towards the CEM–AEM interface, where they recombine with H^+ obtained from the anodic water electrolysis and transported by the CEM to form water and CO_2. Experiments showed the absence of CO_2 gas in the anode electrode, implying that the gas formed at the AEM–CEM interface diffuses back to the cathode compartment, thus successfully inhibiting net CO_2 crossover, as

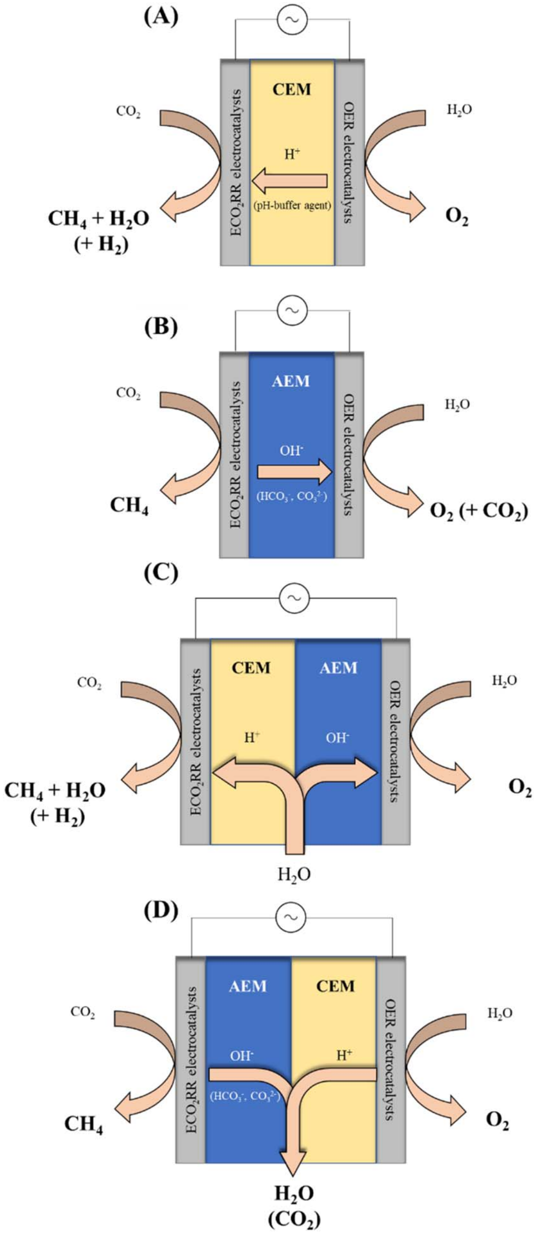

Fig. 9 Schematic representation of an ion exchange membrane in CO_2 electrolyzers. (A) Cation exchange membrane (CEM)-type electrolyzer, (B) anion exchange membrane (AEM)-type electrolyzer, (C) reverse bias bipolar membrane (RB-BPM)-type electrolyzer and (D) forward bias bipolar membrane (FB-BPM)-type electrolyzer.

observed in Fig. 10A.[165] However, it is important to note that this suppression of CO_2 crossover may not always be at play. The CO_2 generated at the BPM junction can also diffuse towards the anode, where it accumulates and transitions into the gas phase at the membrane–anode catalyst layer interface.[181] Over time, this accumulation can lead to structural damage, including catalyst layer perforation and BPM delamination, raising concerns about the stability of BPMs in CO_2 electrolyzers.[181,182] Nevertheless, larger current densities were obtained for the FB-BPM configuration (-150 mA cm^{-2} at 1.7 V) compared to those of the RB-BPM (-80 mA cm^{-2}) using the same cell components (Fig. 10B). Additionally, at a fixed current density of -100 mA cm^{-2}, a higher selectivity towards CO was obtained with the FB-BPM configuration ($\approx$6%, compared to $\approx$ 4% for the AEM or RB-BPM – Fig. 10C).[165] The stability of this FB mode was also measured at 50 mA cm^{-2}, revealing a substantial decrease in CO selectivity within the first 5 h due to water accumulation at the cathode, which progressively blocked CO_2 diffusion towards the electrocatalyst. However, after drying the cathode electrode for 24 h, the CO selectivity returned again to the initial values, confirming that excess water was responsible for the blockage (operation 2, blue region in Fig. 10D).[165]

In another study in which 1 M KOH was fed at the anode, it was shown that the dominant ion transport mechanism is water dissociation at the layer's interface in RB mode,[183] while the absence of water dissociation in FB mode reduces the applied voltage by around 3 V.[183] However, after an operation time of 10 min, a drop in the cathodic potential is observed, which correlates with a decrease in CO selectivity. The authors hypothesize that this effect is due to the formation of potassium-based (bi)carbonate at the AEL–CEL interface.[183]

It is worth pointing out that the FB-BPM configuration is significantly less studied than AEM or CEM CO_2 electrolysis, as it has only been under study for a few years. In particular, studies on the use of BPMs for the CO_2RR have only been published since 2016,[184,185] while FB-BPM research dates back to 2021,[183,186] highlighting the novelty of this approach. In general, only a few studies have focused on the development of BPMs for CO_2 electrolyzers since then, but interesting results have already been obtained. BPMs have quickly achieved similar FEs and current densities to AEM and CEM. In such a short period, a few studies have reported FE_{CO} values of 80–100% at 100–300 mA cm^{-2}.[187–189] We therefore believe that bipolar membranes possess the greatest potential for improvement due to their very early stage of development, but substantial advancements are still needed to render them fully applicable, especially with regard to their stability.

4.2 CO_2 electrolyzers

The design of the CO_2 electrolyzer plays a crucial role in determining the overall performance of the electrochemical reaction, as it directly affects mass transport, ion management, and the system's stability. Different electrolyzer configurations have been developed to address key challenges such as achieving high current densities, optimizing gas–liquid interactions, and ensuring long-term operational stability.

CO_2 electrolyzers can be broadly classified into three main categories (Fig. 11):[190] H-type and parallel plate cells, flow cells and zero-gap cells. In the following sections, each of these electrolyzer types will be discussed in detail, highlighting their operating principles, advantages, limitations and recent advancements.

4.2.1. H- and parallel-plate cell. H- and parallel-plate type electrolyzers are broadly used as lab-scale reactors for ECO_2RR studies due to their straightforward operation and simplicity. Both electrolyzers consists of a two-compartment electrochemical cell, where the cathode electrode is set in one

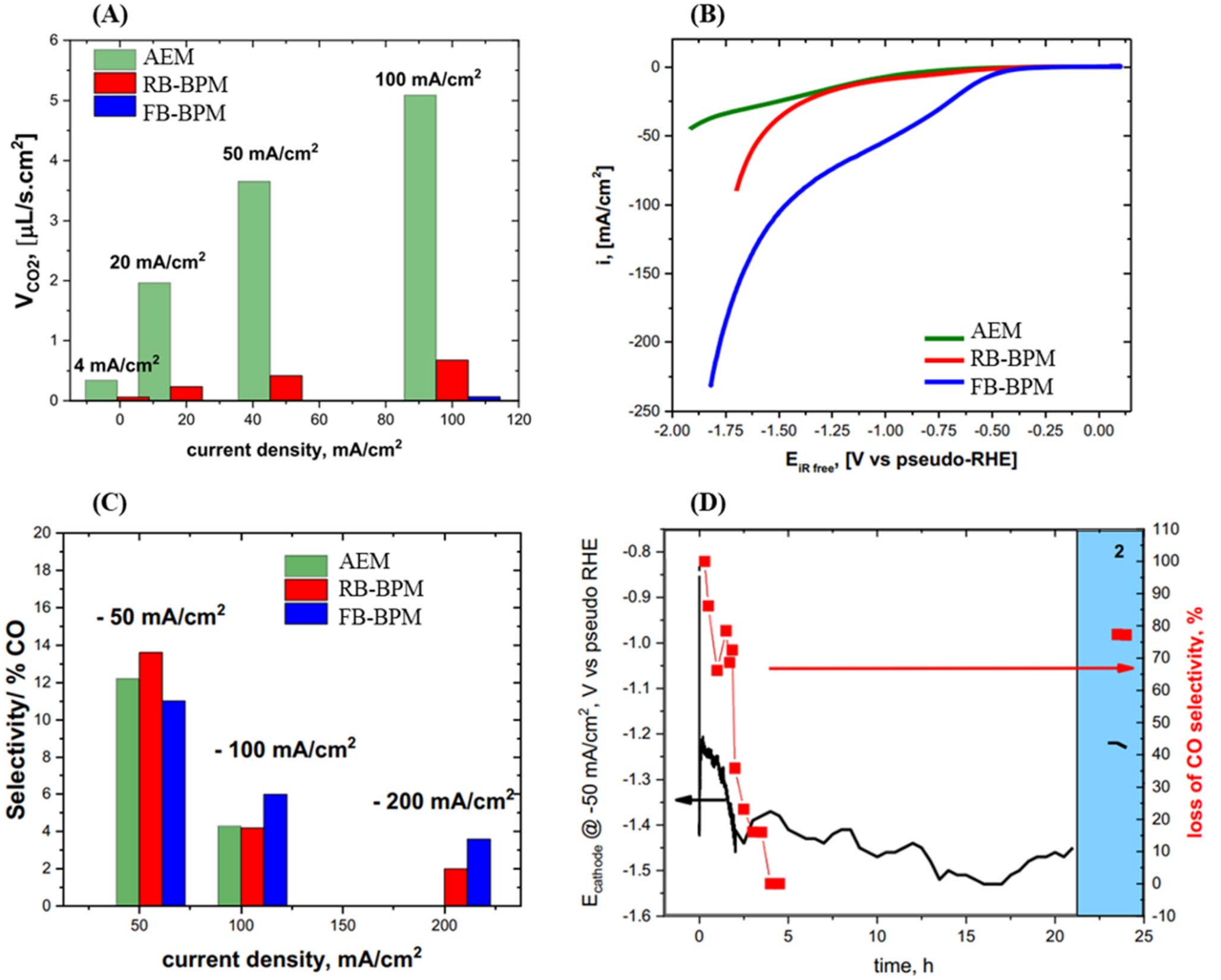

Fig. 10 (A) Volume flows of CO_2 produced on the anode side of a CO_2-electrolyzer cell with an Au-based cathode and an IrO_2–TiO_2 anode catalyst using different membrane configurations. The anode gas composition was analyzed using mass spectrometry at various cell current densities in galvanostatic mode. Cells were operated at 40 °C under ambient pressure. The cathode was fed with pure, humified CO_2 and the anode with humidified Ar. (B) Cathode polarization curves of CO_2-electrolysis cells with an AEM (Fumasep AA30), RB-BPM (Fumatech FBM, 130 µm thickness), and FB-BPM (Fumatech FBM, 130 µm thickness) at 50 mV s^{-1}, 40 °C and ambient pressure. (C) CO selectivities obtained in galvanostatic experiments at various fixed current densities. (D) Chronoamperometric measurements at − 50 mA cm^{-2} (black line) and corresponding CO selectivity measured by *online* MS (red data) for the FB-BPM. The cathode was fed with 50/50 vol% CO_2/Ar, while the anode consisted of a Pt/C catalyst fed with pure H_2. Reproduced from ref. 165 with permission from ECS, copyright 2019.

compartment and the anode and reference electrodes are located in the other.[171,176,191,192] These cathodic and anodic compartments are separated by an IEM, which prevents the crossover and possible recombination of products during operation. During electrolysis, CO_2 gas is continuously fed into the cathodic reservoir solution, where it is reduced on the electrode surface. The gas output is subsequently directed to a gas chromatograph or a mass spectrometer for accurate product analysis and quantification. Liquid products, such as CH_3OH, are collected from the cathode compartment electrolyte post-reaction and analyzed using techniques such as nuclear magnetic resonance or high-performance liquid chromatography.

This electrolyzer design mainly relies on the dissolution of CO_2 into the cathode compartment electrolyte, whereby the use of a liquid solution limits the concentration of CO_2 and its accessibility to the electrode surface. More precisely, aqueous electrolytes possess a CO_2 solubility of ≈30 mM, which restricts the attainable current densities to values <<100 mA cm^{-2} that cannot be considered as industrially relevant.[171,193]

Instead, H- and parallel plate type CO_2 electrolyzers serve as effective tools for evaluating the kinetics of ECO_2RR electrocatalysts, which is in turn extremely useful when comparing the catalytic performance of different materials. However, this cell design is not up-scalable due to its high electric resistance (typically around 5 Ω cm^2 (ref. 194)), inefficient mass transfer and low CO_2 solubility, which as discussed above severely limit the currents attainable with such setups. As shown in Table 2, the highest current densities reported with the H-type cell design rarely surpass 40 mA cm^{-2}, and stability tests typically

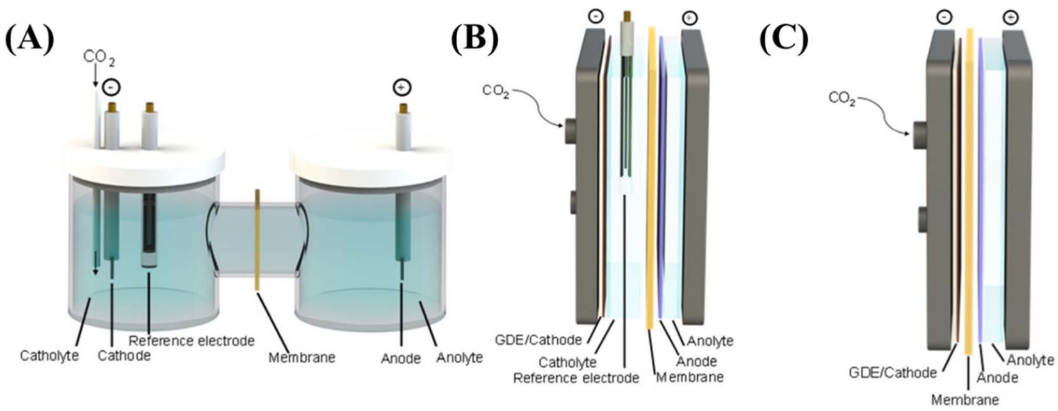

Fig. 11 Schematic illustration of different CO_2 electrolyzers: (A) H-type cell, (B) flow cell, and (C) zero-gap cell. Reproduced from ref. 190 with permission from the American Chemical Society, copyright 2024.

extend only for a few hours. Since this type of reactor is designed exclusively for the fundamental evaluation of catalyst potential, it is not meaningful to perform long-term durability studies, as H-type cells are not envisioned for industrial implementation. Therefore, degradation processes of membranes, catalysts, or other cell components are generally not investigated in these systems.

4.2.2. Flow cell CO_2 electrolyzers. In light of the limitations of H-type electrolyzers, flow cells have emerged as a promising solution to enhance CO_2 mass transfer.[195] These cells are structured into three compartments: a gas chamber, a cathodic compartment and an anodic compartment. The cathode electrode is typically constructed with a porous carbon gas diffusion layer (GDL) coated with the ECO_2RR electrocatalyst, located between the gas chamber and the cathodic compartment.[196] Moreover, an ion-exchange membrane separates cathode and anode electrolytes.[156] In contrast to the conventional H-type CO_2 electrolyzer, the gas diffusion medium provides pathways for gaseous CO_2 to directly access the cathode catalyst layer, thus avoiding the above discussed limitations in CO_2 availability intrinsic to its provision as a dissolved species in the electrolyte. As such, the electrolyte in the cathode compartment is also in contact with the ECO_2RR electrocatalysts, so that the electrochemical reduction of CO_2 proceeds at a solid–liquid–gas interface. This design substantially improves mass transport efficiency and enables higher currents, particularly for the production of CO,[197–200] for which current densities of 500 – 1000 mA cm^{-2} with catalysts of different chemical compositions (Ni-, Co-, Cu- or Fe-based, among others) and electrolytes (such as CO_2-saturated $KHCO_3$ or KOH solutions) have been demonstrated.[197–200] Furthermore, additional studies have shown the potential for hydrocarbon production when selecting appropriate Cu-based electrocatalysts, with current densities reaching more than 1000 mA cm^{-2}.[201–205]

Concerning electrochemical CO_2-to-CH_4 conversion, flow cells have demonstrated large current densities with high CH_4 FE. As previously described, Cu nanoparticles supported on N-doped carbon materials were found to exhibit excellent catalytic performance for the ECO_2RR to CH_4.[88] The electrolyzer configuration consisted of an anion exchange membrane separating anodic and cathodic chambers. For electrochemical measurements, 1 M KOH was used as the electrolyte. At −1.1 V *vs.* RHE, the FE towards CH_4 formation was around 70% with a current density of 230 mA cm^{-2}.[88] As demonstrated in the following section, the authors also conducted electrochemical measurements in zero-gap cells, with lower FEs but long stability (50 h). Additionally, a Cu(I)-based coordination polymer (NNU-33(S)) underwent a substitution of hydroxyl radicals for sulfate radicals during the ECO_2RR that resulted in an *in situ* dynamic crystal structure transformation to NNU-33(H), which reached a current density of 391 mA cm^{-2} with a FE towards CH_4 of 82% at −0.9 V *vs.* RHE.[206] These results were obtained in a 1 M KOH solution and slightly decreased to 350 mA cm^{-2} and 75% after 5 h of continuous electroconversion.

Despite these encouraging results, there are still big challenges for the widespread implementation of large-scale CO_2 flow cells. One notable issue involves the flooding of the electrolyte in the GDL at the cathode gas chamber, causing channel blockages that limit CO_2 transfer from the gas chamber to the catalyst layer. This limitation significantly impacts the ECO_2RR performance and leads to increased HER selectivity after only a few hours of operation.[176,207] Furthermore, many of the used electrolytes, especially KOH, tend to produce carbonates and bicarbonates that precipitate during operation, hindering again the exposure to CO_2 through the blockage of the diffusion channels.[208] To address the flooding issue, three main strategies have been proposed.[209] The first is the control of the interface at the GDL catalyst by using polymeric or hydrophobic substrates that reduce wettability and limit water penetration. The second is to design GDLs with adapted structures that allow excess electrolyte to drain through the electrode and be carried out of the cell with the gas flow. A third approach involves tuning the membrane thickness and CO_2 feed conditions (*i.e.* humidity) to control water transport and minimize salt precipitation.[210,211]

4.2.3. Zero-gap cells. The high resistance caused by the liquid electrolytes circulated between the cathode and the anode in flow cells lowers the overall energy efficiency of these electrochemical systems.[208] Alternatively, zero-gap cells, also known as catholyte-free or membrane electrode assembly (MEA) cells, have been developed to eliminate the liquid electrolyte in the cathode compartment, thus addressing issues such as electrode flooding and ohmic resistance. The ohmic resistance is significantly reduced, reaching values as low as 0.3 Ω cm^2.[212] The zero-gap cell consists of a compact, sandwich-like design with the anode and cathode separated only by an IEM. One of the most promising qualities of zero-gap cells is the scalability of MEA technology, as multiple individual MEA cells can be assembled into a CO_2 electrolyzer stack, making it extremely relevant for industrial-scale processes.[208] In zero-gap cells, gaseous CO_2 (often humidified to enhance the membrane's ionic conductivity) is fed into the cathode through a GDE, and the anode electrode is exposed to the electrolyte. It is worth mentioning that zero-gap cells equipped with AEMs are the most commonly used configuration.[116,175]

Few studies have addressed CO_2 conversion to CH_4 in zero-gap cells. The previously mentioned work about Cu nanoparticles supported on N-doped carbon materials showed a CH_4 selectivity above 70% at −230 mA cm^{-2} in a flow cell reactor.[88] However, this methane FE dropped below 60% after conducting measurements at the same current density in a CO_2 zero-gap electrolyzer. Both CO_2 electrolyzers employed an anion exchange membrane. Nevertheless, it is worth pointing out that the CH_4 selectivity and the current density in a zero-gap cell did not change substantially for 50 h at a voltage of 4 V, indicating excellent stability.

Another exciting study can be found about electrochemical CO_2 conversion into CH_4 in zero-gap cells, using again Cu nanoparticles in a MEA configuration with an anion-exchange membrane.[175] The authors demonstrated that low coordination number Cu nanoparticles are beneficial for reducing the hydrogenation energy requirement towards CH_4 production under alkaline conditions, counteracting the traditionally low energy requirements for C–C coupling. This MEA–catalyst combination operated for 110 h at a current density of 190 mA cm^{-2} with an average FE for CH_4 of 56%, which is the longest operating time for CO_2-to-CH_4 conversion so far.

Despite these advantages, one of the most critical challenges of the zero-gap systems is the precipitation of carbonates and bicarbonates within the catalyst layer and the GDL. Salt precipitation originates from the interplay of CO_2, hydroxide ions and alkali cations (from the anolyte). Carbonates and bicarbonates accumulate within the catalyst layer, GDL and membrane, progressively blocking gas transport, increasing cell resistance and leading to higher HER selectivity. While dilute electrolytes greatly improve stability, as demonstrated by thousands of hours of continuous operation at moderate current densities,[213,214] they also increase cell resistance and limit performance at higher currents. This means that operating without cations prevents precipitation but drastically lowers activity.[213,214] Beyond avoiding precipitation, other strategies aim to remove salts once formed, typically through regeneration protocols. In these approaches, solvents are periodically injected into the cathode to dissolve the precipitated carbonates and restore CO_2 transport, although this inevitably complicates system operation and questions the viability for continuous industrial processes.[215] In the same line, some authors have proposed electrochemical pulse strategies, where the applied potential is periodically altered to redistribute ions and reverse salt precipitation.[215] Alternating between cell potentials of −3.8 V during operation and −2.0 V during regeneration enabled a 15-fold increase in stability compared to continuous operation without regeneration.[215]

5 Future perspectives

A comprehensive overview of the historical and current landscape of the electrochemical CO_2 reduction reaction has been provided in this review, with particular attention to electrochemical CO_2-to-CH_4 conversion. The ECO_2RR emerges as a straightforward solution for mitigating anthropogenic CO_2 in the atmosphere while producing value-added products. CH_4, among all CO_2-derived products, has arisen as a promising chemical due to the already existing industrial infrastructure for its rapid implementation and utilization. Technoeconomic analyses underscore the near-term viability of electrochemical CO_2-to-CH_4 conversion, although significant improvements are imperative to compete effectively with traditional CH_4 synthetic routes. The design of electrocatalysts and advancements in CO_2 electrolyzers stand as crucial milestones in the competitiveness of the ECO_2RR. Future perspectives and challenging targets for the successful implementation of electrochemical CO_2-to-CH_4 conversion are outlined below.

- Metal electrocatalysts, in our assessment, hold promise for the near-term advancement in electrochemical CO_2-to-CH_4 conversion due to their competitive performance. Using Cu as the active site has proven to be the most straightforward strategy to obtain high selectivity towards CH_4 production. However, special emphasis should be placed on tuning the chemical environment of Cu with other metal electrocatalysts to enhance selectivity in CH_4 production.
- Understanding why active sites, such as CuN_4, exhibit such varied selectivity in the ECO_2RR remains a challenge. Cu single atoms have demonstrated remarkable selectivity towards CH_4, CH_3OH and CO, with FE above 70%, in similar carbon materials. Nonetheless, comprehending the disparities in ECO_2RR results among studies using comparable materials remains elusive. We understand that most of the studies in electrocatalyst design prioritize outcomes over delving into the chemistry involved; however, fine chemistry is clearly playing a definitive role in ECO_2RR activity and selectivity. To design better electrocatalysts, the understanding of electrochemistry that is behind these results is imperative.
- Metal-free carbon-based electrocatalysts have been proposed as promising materials for the ECO_2RR. However, their ECO_2RR performance is still far from competitive results. Despite its promising perspective, further efforts are still mandatory for carbon materials to compete with the state-of-the-art metal-containing electrocatalysts.
- Although DFT is often used to support experimental data with contrasted theory methods, its usage is often biased and partial. Authors typically focus solely on determining the electrocatalytic mechanisms that align with experimental

results, disregarding potential alternative reaction pathways. Here, the complexity of evaluating all potential mechanisms is worth noting, given the varied possibilities in the ECO_2RR. However, we believe that it is crucial to emphasize that DFT results, as presented in these studies, should not be regarded as absolute truths but rather as thermodynamic validations of specific ECO_2RR routes.

- Faradaic efficiency (FE) denotes selectivity towards a particular product in the ECO_2RR. Despite the emphasis on FE in numerous studies, there must exist a crucial need to place greater scrutiny on energy efficiency (EE). EE, expressing the FE per voltage efficiency, provides a more meticulous indicator, especially for techno-economic aspects. In the case of pathways with a high number of electrons transferred, such as CH_4 (8-electron pathway), high voltages are usually required to obtain high selectivity. This is not reflected in FE but becomes essential in EE.

- We noticed a significant gap between fundamental and cell design researchers, which needs to be overcome to fulfill the cost and energy requirements for the electrochemical conversion of CO_2 into not only CH_4, but all CO_2-derived products. Fundamental research is imperative for understanding kinetics and thermodynamics, while producing the most active ECO_2RR electrocatalysts but lacks practical applications. On the other hand, design of highly efficient electrochemical cells is useless if state-of-the-art electrocatalysts cannot be used in them.

- Advancements in CO_2 electrolyzers are crucial to bringing electrochemical CO_2-to-CH_4 to competitive levels. H-type electrolyzers are useful electrochemical devices that provide valuable insights into mechanisms and fundamentals when comparing different electrocatalysts. However, the limited solubility of CO_2 in aqueous solution hampers the industrial applications of these devices. More attention should be directed to flow or zero-gap electrolyzers, capable of providing current densities above 100 mA cm^{-2}.

- Progress in ion exchange membranes is essential for the future electrochemical production of CH_4 from CO_2. Both CEMs and AEMs have been widely studied in CO_2 electrolysis, showing significant drawbacks that hinder their worldwide application. CEMs exhibit high HER activity in the cathode electrode, which reduces the ECO_2RR selectivity. At the same time, AEMs display a large crossover issue, allowing CO_2products to cross the membranes and recombine at the anode electrode, reducing the energy efficiency.

- Recently, BPMs have emerged as a promising alternative to mitigate crossover and pH challenges. However, the low stability under working conditions remains a key factor for the feasibility of these membranes. Particular relevance should be given to FB-BPMs, as despite their novelty, they have reached comparable current densities to AEMs and RB-BPMs. Moreover, in alignment with technoeconomic assessments, BPMs are postulated as the most feasible membranes for the next generation of flow electrolyzers.

Conflicts of interest

The authors declare no competing financial interest.

Data availability

No primary research results, software or code have been included and no new data were generated or analyzed as part of this review.

Acknowledgements

This work was financially supported by the Swiss Center of Excellence on Net Zero Emissions (SCENE) of the ETH domain.

References

1 Broken record, **http://www.climate.gov/news-features/feed/broken-record-atmospheric-carbon-dioxide-levels-jump-again**, accessed November 20, 2023.
2 CO_2 levels in atmosphere at their highest in 800,000 years, **https://www.weforum.org/agenda/2018/05/earth-just-hit-a-terrifying-milestone-for-the-first-time-in-more-than-800-000-years/**, accessed November 20, 2023.
3 A. Mikhaylov, N. Moiseev, K. Aleshin and T. Burkhardt, *Entrep. Sustain. Issues*, 2020, **7**, 2897–2913.
4 S. Fawzy, A. I. Osman, J. Doran and D. W. Rooney, *Environ. Chem. Lett.*, 2020, **18**, 2069–2094.
5 J. Jiang, L. Cao, X. Jin, Z. Yu, H. Zhang, J. Fu and G. Jiang, *J. Environ. Sci.*, 2023, **140**, 79–90.
6 P. M. Cox, R. A. Betts, C. D. Jones, S. A. Spall and I. J. Totterdell, *Nature*, 2000, **408**, 184–187.
7 T.-Z. Ang, M. Salem, M. Kamarol, H. S. Das, M. A. Nazari and N. Prabaharan, *Energy Strategy Rev.*, 2022, **43**, 100939.
8 M. Shahbaz, C. Raghutla, K. R. Chittedi, Z. Jiao and X. V. Vo, *Energy*, 2020, **207**, 118162.
9 E. T. Sayed, A. G. Olabi, A. H. Alami, A. Radwan, A. Mdallal, A. Rezk and M. A. Abdelkareem, *Energies*, 2023, **16**, 1415.
10 D. M. D'Alessandro, B. Smit and J. R. Long, *Angew. Chem., Int. Ed.*, 2010, **49**, 6058–6082.
11 W. Gao, S. Liang, R. Wang, Q. Jiang, Y. Zhang, Q. Zheng, B. Xie, C. Y. Toe, X. Zhu, J. Wang, L. Huang, Y. Gao, Z. Wang, C. Jo, Q. Wang, L. Wang, Y. Liu, B. Louis, J. Scott, A.-C. Roger, R. Amal, H. He and S.-E. Park, *Chem. Soc. Rev.*, 2020, **49**, 8584–8686.
12 Y. Chen, C. Liu, S. Guo, T. Mu, L. Wei and Y. Lu, *Green Energy Environ.*, 2022, **7**, 394–410.
13 L.-Q. Qiu, X. Yao, Y.-K. Zhang, H.-R. Li and L.-N. He, *J. Org. Chem.*, 2023, **88**, 4942–4964.
14 S. Gulati, S. Vijayan, Mansi, S. Kumar, B. Harikumar, M. Trivedi and R. S. Varma, *Coord. Chem. Rev.*, 2023, **474**, 214853.
15 S. A. Mazari, N. Hossain, W. J. Basirun, N. M. Mubarak, R. Abro, N. Sabzoi and A. Shah, *Process Saf. Environ. Prot.*, 2021, **149**, 67–92.
16 C. G. Okoye-Chine, K. Otun, N. Shiba, C. Rashama, S. N. Ugwu, H. Onyeaka and C. T. Okeke, *J. CO2 Util.*, 2022, **62**, 102099.
17 A. D. N. Kamkeng, M. Wang, J. Hu, W. Du and F. Qian, *Chem. Eng. J.*, 2021, **409**, 128138.

18 R. Gupta, A. Mishra, Y. Thirupathaiah and A. K. Chandel, *Biomass Convers. Biorefinery*, 2022, **14**, 3007–3030.

19 Y. Ma, S. Wang and X. Duan, *Chem. Eng. J.*, 2023, **455**, 140654.

20 D. Li, M. Kassymova, X. Cai, S.-Q. Zang and H.-L. Jiang, *Coord. Chem. Rev.*, 2020, **412**, 213262.

21 T. Kong, Y. Jiang and Y. Xiong, *Chem. Soc. Rev.*, 2020, **49**, 6579–6591.

22 Y. Y. Birdja, E. Pérez-Gallent, M. C. Figueiredo, A. J. Göttle, F. Calle-Vallejo and M. T. M. Koper, *Nat. Energy*, 2019, **4**, 732–745.

23 E. V. Kondratenko, G. Mul, J. Baltrusaitis, G. O. Larrazábal and J. Pérez-Ramírez, *Energy Environ. Sci.*, 2013, **6**, 3112–3135.

24 S. Nitopi, E. Bertheussen, S. B. Scott, X. Liu, A. K. Engstfeld, S. Horch, B. Seger, I. E. L. Stephens, K. Chan, C. Hahn, J. K. Nørskov, T. F. Jaramillo and I. Chorkendorff, *Chem. Rev.*, 2019, **119**, 7610–7672.

25 J. Chen and L. Wang, *Adv. Mater.*, 2022, **34**, 2103900.

26 G. H. Han, J. Bang, G. Park, S. Choe, Y. J. Jang, H. W. Jang, S. Y. Kim and S. H. Ahn, *Small*, 2023, **19**, 2205765.

27 M. Li, H. Wang, W. Luo, P. C. Sherrell, J. Chen and J. Yang, *Adv. Mater.*, 2020, **32**, 2001848.

28 Z. Gao, J. Li, Z. Zhang and W. Hu, *Chin. Chem. Lett.*, 2022, **33**, 2270–2280.

29 W. Lai, Y. Qiao, Y. Wang and H. Huang, *Adv. Mater.*, 2023, **35**, 2306288.

30 H. Zheng, Z. Yang, X. Kong, Z. Geng and J. Zeng, *Chin. J. Catal.*, 2022, **43**, 1634–1641.

31 V. S. S. Mosali, A. M. Bond and J. Zhang, *Nanoscale*, 2022, **14**, 15560–15585.

32 U. Mustapha, C. C. Nnadiekwe, M. A. Alhaboudal, U. Yunusa, A. S. Abdullahi, I. Abdulazeez, I. Hussain, S. A. Ganiyu, A. A. Al-Saadi and K. Alhooshani, *J. Energy Chem.*, 2023, **85**, 198–219.

33 R. Zhao, P. Ding, P. Wei, L. Zhang, Q. Liu, Y. Luo, T. Li, S. Lu, X. Shi, S. Gao, A. M. Asiri, Z. Wang and X. Sun, *Adv. Funct. Mater.*, 2021, **31**, 2009449.

34 K. Lacroix, M. H. Goldberg, A. Gustafson, S. A. Rosenthal and A. Leiserowitz, *J. Environ. Psychol.*, 2021, **77**, 101671.

35 R. W. Howarth, A. Ingraffea and T. Engelder, *Nature*, 2011, **477**, 271–275.

36 X. Wang, A. Xu, F. Li, S.-F. Hung, D.-H. Nam, C. M. Gabardo, Z. Wang, Y. Xu, A. Ozden, A. S. Rasouli, A. H. Ip, D. Sinton and E. H. Sargent, *J. Am. Chem. Soc.*, 2020, **142**, 3525–3531.

37 *The High Purity Methane Gas Market, Industry Size Forecast*, **https://www.marketsandmarkets.com/Market-Reports/high-purity-methane-gas-market-258569778.html**, accessed November 17, 2023.

38 *Carbon Monoxide Market Size, Share & COVID-19 Impact Analysis, by Application (Metal Fabrication, Chemicals, Ore Processing & Extraction, Pharma & Biotechnology and Electronics) and Regional Forecast, 2023-2030*, 2022, **https://www.fortunebusinessinsights.com/u-s-carbon-monoxide-market-108572**, accessed November 20, 2023.

39 M. R. F. https://www.marketresearchfuture.com, Formic Acid Market Size, Share, Growth | Report, 2030, **https://www.marketresearchfuture.com/reports/formic-acid-market-1132**, accessed November 17, 2023.

40 A. J. Welch, I. A. Digdaya, R. Kent, P. Ghougassian, H. A. Atwater and C. Xiang, *ACS Energy Lett.*, 2021, **6**, 1540–1549.

41 Y. Zheng, Y. Wang, Y. Yuan and H. Huang, *ChemNanoMat*, 2021, **7**, 502–514.

42 Z. Sun, T. Ma, H. Tao, Q. Fan and B. Han, *Chem*, 2017, **3**, 560–587.

43 W. Choi, D. H. Won and Y. J. Hwang, *J. Mater. Chem. A*, 2020, **8**, 15341–15357.

44 J. Qu, X. Cao, L. Gao, J. Li, L. Li, Y. Xie, Y. Zhao, J. Zhang, M. Wu and H. Liu, *Nano-Micro Lett.*, 2023, **15**, 178.

45 X. Li, X. Wu, X. Lv, J. Wang and H. B. Wu, *Chem Catal.*, 2022, **2**, 262–291.

46 W. Xi, P. Yang, M. Jiang, X. Wang, H. Zhou, J. Duan, M. Ratova and D. Wu, *Appl. Catal. B Environ.*, 2024, **341**, 123291.

47 F. Pan and Y. Yang, *Energy Environ. Sci.*, 2020, **13**, 2275–2309.

48 R. Kortlever, J. Shen, K. J. P. Schouten, F. Calle-Vallejo and M. T. M. Koper, *J. Phys. Chem. Lett.*, 2015, **6**, 4073–4082.

49 X. Nie, M. R. Esopi, M. J. Janik and A. Asthagiri, *Angew. Chem., Int. Ed.*, 2013, **52**, 2459–2462.

50 M. M. Waegele, C. M. Gunathunge, J. Li and X. Li, *J. Chem. Phys.*, 2019, **151**, 160902.

51 J. H. Bae, J.-H. Han and T. D. Chung, *Phys. Chem. Chem. Phys.*, 2011, **14**, 448–463.

52 J. Wu, *Chem. Rev.*, 2022, **122**, 10821–10859.

53 J. Yu, J. Yin, R. Li, Y. Ma and Z. Fan, *Chem Catal.*, 2022, **2**, 2229–2252.

54 J. Resasco, L. D. Chen, E. Clark, C. Tsai, C. Hahn, T. F. Jaramillo, K. Chan and A. T. Bell, *J. Am. Chem. Soc.*, 2017, **139**, 11277–11287.

55 A. Murata and Y. Hori, *Bull. Chem. Soc. Jpn.*, 1991, **64**, 123–127.

56 F. Ni, K. Jia, Y. Chen, Y. Wen and S. He, *Mater. Chem. Front.*, 2023, **7**, 2750–2763.

57 T. Luo, K. Liu, J. Fu, S. Chen, H. Li, H. Pan and M. Liu, *Adv. Energy Sustain. Res.*, 2023, **4**, 2200148.

58 B. Pan, Y. Wang and Y. Li, *Chem Catal.*, 2022, **2**, 1267–1276.

59 Y. Wang, J. Liu, Y. Wang, A. M. Al-Enizi and G. Zheng, *Small*, 2017, **13**, 1701809.

60 T. Tang, Z. Wang and J. Guan, *Adv. Funct. Mater.*, 2022, **32**, 2111504.

61 X. She, Y. Wang, H. Xu, S. Chi Edman Tsang and S. Ping Lau, *Angew. Chem., Int. Ed.*, 2022, **61**, e202211396.

62 S. R. Hui and P. De Luna, *Matter*, 2021, **4**, 1555–1577.

63 H. Xie, T. Wang, J. Liang, Q. Li and S. Sun, *Nano Today*, 2018, **21**, 41–54.

64 S.-T. Gao, S.-Q. Xiang, J.-L. Shi, W. Zhang and L.-B. Zhao, *Phys. Chem. Chem. Phys.*, 2020, **22**, 9607–9615.

65 J. J. Kim, D. P. Summers and K. W. Frese, *J. Electroanal. Chem. Interfacial Electrochem.*, 1988, **245**, 223–244.

66 H. Mistry, A. S. Varela, C. S. Bonifacio, I. Zegkinoglou, I. Sinev, Y.-W. Choi, K. Kisslinger, E. A. Stach, J. C. Yang, P. Strasser and B. R. Cuenya, *Nat. Commun.*, 2016, **7**, 12123.

67 S. Lee, D. Kim and J. Lee, *Angew. Chem.*, 2015, **127**, 14914–14918.

68 D. Kim, S. Lee, J. D. Ocon, B. Jeong, J. K. Lee and J. Lee, *Phys. Chem. Chem. Phys.*, 2014, **17**, 824–830.

69 R. Reske, H. Mistry, F. Behafarid, B. Roldan Cuenya and P. Strasser, *J. Am. Chem. Soc.*, 2014, **136**, 6978–6986.

70 M. He, X. Chang, T.-H. Chao, C. Li, W. A. I. Goddard, M.-J. Cheng, B. Xu and Q. Lu, *ACS Catal.*, 2022, **12**, 6036–6046.

71 K. Manthiram, B. J. Beberwyck and A. P. Alivisatos, *J. Am. Chem. Soc.*, 2014, **136**, 13319–13325.

72 P. Chauhan, K. Hiekel, J. S. Diercks, J. Herranz, V. A. Saveleva, P. Khavlyuk, A. Eychmüller and T. J. Schmidt, *ACS Mater. Au*, 2022, **2**, 278–292.

73 S. Li, S. Li, Z. Wu, L. Qin, J. Liu, W. Zhou, H. Kang, L. Gong and L. Zhang, *Fuel*, 2024, **357**, 129760.

74 T. L. Soucy, W. S. Dean, J. Zhou, K. E. Rivera Cruz and C. C. L. McCrory, *Acc. Chem. Res.*, 2022, **55**, 252–261.

75 C. Ampelli, C. Genovese, S. Perathoner, G. Centi, M. Errahali, G. Gatti and L. Marchese, *Chem. Eng. Trans.*, 2014, **41**, 13–18.

76 H. Wu, M. Zeng, X. Zhu, C. Tian, B. Mei, Y. Song, X.-L. Du, Z. Jiang, L. He, C. Xia and S. Dai, *ChemElectroChem*, 2018, **5**, 2717–2721.

77 G. Lu, H. Zheng, J. Lv, G. Wang and X. Huang, *J. Power Sources*, 2020, **480**, 229091.

78 L. Xue, C. Zhang, J. Wu, Q.-Y. Fan, Y. Liu, Y. Wu, J. Li, H. Zhang, F. Liu and S. Zeng, *Appl. Catal. B Environ.*, 2022, **304**, 120951.

79 K. Chan, C. Tsai, H. A. Hansen and J. K. Nørskov, *ChemCatChem*, 2014, **6**, 1899–1905.

80 Y. Li, Z. Yin, X. Liu, M. Cui, S. Chen and T. Ma, *Mater. Today Chem.*, 2021, **19**, 100411.

81 Y. Ren, X. Sun, K. Qi and Z. Zhao, *Appl. Surf. Sci.*, 2022, **602**, 154211.

82 J. Quílez-Bermejo, S. García-Dalí, A. Daouli, A. Zitolo, R. L. S. Canevesi, M. Emo, M. T. Izquierdo, M. Badawi, A. Celzard and V. Fierro, *Adv. Funct. Mater.*, 2023, **33**, 2300405.

83 J. Quílez-Bermejo, E. Morallón and D. Cazorla-Amorós, *Carbon*, 2020, **165**, 434–454.

84 J. Quílez-Bermejo, S. Pérez-Rodríguez, D. Torres, R. Canevesi, E. Morallón, D. Cazorla-Amorós, A. Celzard and V. Fierro, *J. Colloid Interface Sci.*, 2024, **654**, 446–453.

85 J. Quílez-Bermejo, S. Pérez-Rodríguez, R. Canevesi, D. Torres, E. Morallón, D. Cazorla-Amorós, A. Celzard and V. Fierro, *Carbon*, 2022, **196**, 708–717.

86 G. Alemany-Molina, J. Quílez-Bermejo, M. Navlani-García, E. Morallón and D. Cazorla-Amorós, *Carbon*, 2022, **196**, 378–390.

87 H. Dai, H. Zou, T. Song, L. Gao, S. Wei, H. Liu, H. Xiong, C. Huang and L. Duan, *Inorg. Chem. Front.*, 2023, **10**, 2189–2196.

88 Y. Wu, C. Chen, X. Yan, R. Wu, S. Liu, J. Ma, J. Zhang, Z. Liu, X. Xing, Z. Wu and B. Han, *Chem. Sci.*, 2022, **13**, 8388–8394.

89 B. Zhang, B. Zhang, Y. Jiang, T. Ma, H. Pan and W. Sun, *Small*, 2021, **17**, 2101443.

90 C. Xu, X. Zhi, A. Vasileff, D. Wang, B. Jin, Y. Jiao, Y. Zheng and S.-Z. Qiao, *Small Struct.*, 2021, **2**, 2000058.

91 W. Ju, A. Bagger, G.-P. Hao, A. S. Varela, I. Sinev, V. Bon, B. Roldan Cuenya, S. Kaskel, J. Rossmeisl and P. Strasser, *Nat. Commun.*, 2017, **8**, 944.

92 H. Yang, Y. Wu, G. Li, Q. Lin, Q. Hu, Q. Zhang, J. Liu and C. He, *J. Am. Chem. Soc.*, 2019, **141**, 12717–12723.

93 K. Zhang, J. Xu, T. Yan, L. Jia, J. Zhang, C. Shao, L. Zhang, N. Han and Y. Li, *Adv. Funct. Mater.*, 2023, **33**, 2214062.

94 H. Cheng, X. Wu, X. Li, X. Nie, S. Fan, M. Feng, Z. Fan, M. Tan, Y. Chen and G. He, *Chem. Eng. J.*, 2021, **407**, 126842.

95 R. Purbia, S. Y. Choi, C. H. Woo, J. Jeon, C. Lim, D. K. Lee, J. Y. Choi, H. S. Oh and J. M. Baik, *Appl. Catal. B Environ.*, 2024, **345**, 123694.

96 W. Cao, D. Yang, B. Li, Y. Mi, K. Oi, Y. Mao, Y. Zhao, H. Li and Z. H. He, *Green Chem.*, 2025, **27**, 9512–9521.

97 R. Bhawnani, R. Sartape, V. Gande, M. Barsoum, E. Kallon, R. dos Reis, V. Dravid and M. Singh, *Small*, 2025, **21**, 2408010.

98 Y. Dai, H. Li, C. Wang, W. Xue, M. Zhang, D. Zhao, J. Xue, J. Li, L. Luo, C. Liu, X. Li, P. Cui, Q. Jiang, T. Zheng, S. Gu, Y. Zhang, J. Xiao, C. Xia and J. Zeng, *Nat. Commun.*, 2023, **14**, 3382.

99 Y. Wang, Z. Chen, P. Han, Y. Du, Z. Gu, X. Xu and G. Zheng, *ACS Catal.*, 2018, **8**, 7113–7119.

100 Y. Cai, J. Fu, Y. Zhou, Y.-C. Chang, Q. Min, J.-J. Zhu, Y. Lin and W. Zhu, *Nat. Commun.*, 2021, **12**, 586.

101 C. Yin, Q. Li, J. Zheng, Y. Ni, H. Wu, A.-L. Kjøniksen, C. Liu, Y. Lei and Y. Zhang, *Adv. Powder Mater.*, 2022, **1**, 100055.

102 J. Zhao, P. Zhang, T. Yuan, D. Cheng, S. Zhen, H. Gao, T. Wang, Z.-J. Zhao and J. Gong, *J. Am. Chem. Soc.*, 2023, **145**, 6622–6627.

103 Y. Shao, Q. Yuan and J. Zhou, *Small*, 2023, **19**, 2303446.

104 A. Guan, Z. Chen, Y. Quan, C. Peng, Z. Wang, T.-K. Sham, C. Yang, Y. Ji, L. Qian, X. Xu and G. Zheng, *ACS Energy Lett.*, 2020, **5**, 1044–1053.

105 Y. Wang, L. Cheng, Y. Zhu, J. Liu, C. Xiao, R. Chen, L. Zhang, Y. Li and C. Li, *Appl. Catal. B Environ.*, 2022, **317**, 121650.

106 M. Chhetri, M. Wan, Z. Jin, J. Yeager, C. Sandor, C. Rapp, H. Wang, S. Lee, C. J. Bodenschatz, M. J. Zachman, F. Che and M. Yang, *Nat. Commun.*, 2023, **14**, 3075.

107 F. Kong, J. Xie, Z. Lu, J. Hu, Y. Feng and Y. Cao, *Chem. Eng. J.*, 2024, **481**, 148497.

108 X. Zhi, A. Vasileff, Y. Zheng, Y. Jiao and S.-Z. Qiao, *Energy Environ. Sci.*, 2021, **14**, 3912–3930.

109 S. A. Mahyoub, F. A. Qaraah, C. Chen, F. Zhang, S. Yan and Z. Cheng, *Sustain. Energy Fuels*, 2019, **4**, 50–67.

110 S. Singh, R. K. Gautam, K. Malik and A. Verma, *J. CO2 Util.*, 2017, **18**, 139–146.

111 Y. Cui, C. Yang, H. Lin, S. Rui, D. Yao, Y. Liao, C. Zhang, Y. Fang, X. Wang, Z. Zhong, Y. Song, G. Wang, L. Zhuang and Z. Li, *ACS Catal.*, 2023, **13**, 169–178.

112 J. Shen, M. J. Kolb, A. J. Göttle and M. T. M. Koper, *J. Phys. Chem. C*, 2016, **120**, 15714–15721.

113 K. Iwase, K. Ebner, J. S. Diercks, V. A. Saveleva, S. Ünsal, F. Krumeich, T. Harada, I. Honma, S. Nakanishi,

K. Kamiya, T. J. Schmidt and J. Herranz, *ACS Appl. Mater. Interfaces*, 2021, **13**, 15122–15131.

114 X. Wu, J. Y. Zhao, J. W. Sun, W. J. Li, H. Y. Yuan, P. F. Liu, S. Dai and H. G. Yang, *Small*, 2023, **19**, 2207037.

115 R. Ifraemov, S. Mukhopadhyay and I. Hod, *Sol. RRL*, 2023, **7**, 2201068.

116 L. Lin, T. Liu, J. Xiao, H. Li, P. Wei, D. Gao, B. Nan, R. Si, G. Wang and X. Bao, *Angew. Chem., Int. Ed.*, 2020, **59**, 22408–22413.

117 J. Shen, D. Lan and T. Yang, *Int. J. Electrochem. Sci.*, 2018, **13**, 9847–9857.

118 X. Wan, W. Chen, J. Yang, M. Liu, X. Liu and J. Shui, *ChemElectroChem*, 2019, **6**, 304–315.

119 M. Sun, C. Chen, M. Wu, D. Zhou, Z. Sun, J. Fan, W. Chen and Y. Li, *Nano Res.*, 2022, **15**, 1753–1778.

120 Q. Zhang and J. Guan, *Adv. Funct. Mater.*, 2020, **30**, 2000768.

121 J. Quílez-Bermejo, A. Daouli, S. García-Dalí, Y. Cui, A. Zitolo, J. Castro-Gutiérrez, M. Emo, M. T. Izquierdo, W. Mustain, M. Badawi, A. Celzard and V. Fierro, *Adv. Funct. Mater.*, 2024, **34**, 2403810.

122 S. Chen, J. Chen, Y. Li, S. Tan, X. Liao, T. Zhao, K. Zhang, E. Hu, F. Cheng and H. Wang, *Adv. Funct. Mater.*, 2023, **33**, 2300801.

123 C. Jia, Y. Zhao, S. Song, Q. Sun, Q. Meyer, S. Liu, Y. Shen and C. Zhao, *Adv. Energy Mater.*, 2023, **13**, 2302007.

124 K. Yu, K. Sun, W.-C. (Max) Cheong, X. Tan, C. He, J. Zhang, J. Li and C. Chen, *Small*, 2023, **19**, 2302611.

125 W. Ju, A. Bagger, X. Wang, Y. Tsai, F. Luo, T. Möller, H. Wang, J. Rossmeisl, A. S. Varela and P. Strasser, *ACS Energy Lett.*, 2019, **4**, 1663–1671.

126 N. Leonard, W. Ju, I. Sinev, J. Steinberg, F. Luo, A. S. Varela, B. R. Cuenya and P. Strasser, *Chem. Sci.*, 2018, **9**, 5064–5073.

127 K. A. Adegoke and N. W. Maxakato, *Mater. Today Chem.*, 2022, **24**, 100838.

128 S. Liu, H. Yang, X. Su, J. Ding, Q. Mao, Y. Huang, T. Zhang and B. Liu, *J. Energy Chem.*, 2019, **36**, 95–105.

129 A. Dessalle, J. Quílez-Bermejo, V. Fierro, F. Xu and A. Celzard, *Carbon*, 2023, **203**, 237–260.

130 B. Martínez-Sánchez, J. Quílez-Bermejo, D. Cazorla-Amorós and E. Morallón, in *Carbon-Based Metal Free Catalysts*, ed. A. M. A. Asiri, A. Khan, S. A. Bhawani, B. M. M. Abu-Zied, S. Siengchin and H. Džudžević-Čančar, Elsevier, 2022, pp. 213–244.

131 J. Quílez-Bermejo, R. Dupuis, R. Canevesi, K. Ioannidou, A. Celzard, R. Pellenq and V. Fierro, *Carbon*, 2025, **241**, 120383.

132 W. Zhang, B. Jia, X. Liu and T. Ma, *Small*, 2022, **3**, 5–34.

133 J. Quílez-Bermejo, E. Morallón and D. Cazorla-Amorós, *Polymers*, 2020, **12**, 2382.

134 J. Quílez-Bermejo, C. González-Gaitán, E. Morallón and D. Cazorla-Amorós, *Carbon*, 2017, **119**, 62–71.

135 J. Quílez-Bermejo, M. Melle-Franco, E. San-Fabián, E. Morallón and D. Cazorla-Amorós, *J. Mater. Chem. A*, 2019, **7**, 24239–24250.

136 K. Saravanan, E. Gottlieb and J. A. Keith, *Carbon*, 2017, **111**, 859–866.

137 J. Wu, S. Ma, J. Sun, J. I. Gold, C. Tiwary, B. Kim, L. Zhu, N. Chopra, I. N. Odeh, R. Vajtai, A. Z. Yu, R. Luo, J. Lou, G. Ding, P. J. A. Kenis and P. M. Ajayan, *Nat. Commun.*, 2016, **7**, 13869.

138 X. Zou, M. Liu, J. Wu, P. M. Ajayan, J. Li, B. Liu and B. I. Yakobson, *ACS Catal.*, 2017, **7**, 6245–6250.

139 J. Wu, R. M. Yadav, M. Liu, P. P. Sharma, C. S. Tiwary, L. Ma, X. Zou, X.-D. Zhou, B. I. Yakobson, J. Lou and P. M. Ajayan, *ACS Nano*, 2015, **9**, 5364–5371.

140 P. P. Sharma, J. Wu, R. M. Yadav, M. Liu, C. J. Wright, C. S. Tiwary, B. I. Yakobson, J. Lou, P. M. Ajayan and X.-D. Zhou, *Angew. Chem., Int. Ed.*, 2015, **54**, 13701–13705.

141 J. Wu, M. Liu, P. P. Sharma, R. M. Yadav, L. Ma, Y. Yang, X. Zou, X.-D. Zhou, R. Vajtai, B. I. Yakobson, J. Lou and P. M. Ajayan, *Nano Lett.*, 2016, **16**, 466–470.

142 J. Li, W.-Y. Zan, H. Kang, Z. Dong, X. Zhang, Y. Lin, Y.-W. Mu, F. Zhang, X.-M. Zhang and J. Gu, *Appl. Catal. B Environ.*, 2021, **298**, 120510.

143 Y. Zhang, F. Qi and Y. Liu, *RSC Adv.*, 2020, **10**, 11210–11218.

144 X. Bi, F. Zhang, W. Chen, X. Huang, G. Yan, H. Zhao, Z. Yang and Y. Wang, *Appl. Surf. Sci.*, 2023, **638**, 157950.

145 M.-Z. Qin, Y. Bian, H.-Y. Niu, W.-X. Fu, X.-G. Zhang, Q.-Y. Hu, D. Guo, C.-G. Niu and L. Zhang, *Appl. Catal. B Environ.*, 2023, **324**, 122285.

146 Y. Liu, Q. Li, X. Guo, X. Kong, J. Ke, M. Chi, Q. Li, Z. Geng and J. Zeng, *Adv. Mater.*, 2020, **32**, 1907690.

147 S. G. Peera, R. S. Menon, S. K. Das, A. Alfantazi, K. Karuppasamy, C. Liu and A. K. Sahu, *Coord. Chem. Rev.*, 2024, **500**, 215491.

148 T. Kesavan, T. Partheeban, M. Vivekanantha, N. Prabu, M. Kundu, P. Selvarajan, S. Umapathy, A. Vinu and M. Sasidharan, *ACS Appl. Mater. Interfaces*, 2020, **12**, 24007–24018.

149 L. Hu, Q. Shen, X. Yang, X. Wu, R. Luo, X. Wen and Z. Fei, *Energy Fuels*, 2023, **37**, 2394–2400.

150 S. García-Dalí, J. Quílez-Bermejo, J. Castro-Gutiérrez, N. Baccile, M. T. Izquierdo, A. Celzard and V. Fierro, *Carbon*, 2023, **212**, 118154.

151 S. García-Dalí, J. Quílez-Bermejo, J. Castro-Gutiérrez, M. T. Izquierdo, A. Celzard and V. Fierro, *RSC Sustain.*, 2023, **1**, 1270–1277.

152 S. Shaheen Shah, S. M. Abu Nayem, N. Sultana, A. J. Saleh Ahammad and Md. Abdul Aziz, *ChemSusChem*, 2022, **15**, e202101282.

153 G. Ma, G. Ning and Q. Wei, *Carbon*, 2022, **195**, 328–340.

154 Y. Wang, J. Chen, G. Wang, Y. Li and Z. Wen, *Angew. Chem., Int. Ed.*, 2018, **57**, 13120–13124.

155 Y. Zhao, Q. Yuan, M. Fan, A. Wang, K. Sun, Z. Wang and J. Jiang, *Chin. Chem. Lett.*, 2023, **34**, 108120.

156 F. Habibzadeh, P. Mardle, N. Zhao, H. D. Riley, D. A. Salvatore, C. P. Berlinguette, S. Holdcroft and Z. Shi, *Electrochem. Energy Rev.*, 2023, **6**, 26.

157 M. Heßelmann, H. Minten, T. Geissler, R. G. Keller, A. Bardow and M. Wessling, *Adv. Sustain. Syst.*, 2023, **7**, 2300077.

158 C. Delacourt, P. L. Ridgway, J. B. Kerr and J. Newman, *J. Electrochem. Soc.*, 2007, **155**, B42.

159 M. Ersöz, *Sep. Sci. Technol.*, 1995, **30**, 3523–3533.
160 M. Ahmed and I. Dincer, *Int. J. Energy Res.*, 2011, **35**, 1213–1228.
161 T. Tschinder, T. Schaffer, S. D. Fraser and V. Hacker, *J. Appl. Electrochem.*, 2007, **37**, 711–716.
162 D. A. Salvatore, C. M. Gabardo, A. Reyes, C. P. O'Brien, S. Holdcroft, P. Pintauro, B. Bahar, M. Hickner, C. Bae, D. Sinton, E. H. Sargent and C. P. Berlinguette, *Nat. Energy*, 2021, **6**, 339–348.
163 C. Delacourt and J. Newman, *J. Electrochem. Soc.*, 2010, **157**, B1911.
164 C. Delacourt and J. Newman, *J. Electrochem. Soc.*, 2008, **155**, B1210.
165 A. Pătru, T. Binninger, B. Pribyl and T. J. Schmidt, *J. Electrochem. Soc.*, 2019, **166**, F34.
166 B. Pribyl-Kranewitter, A. Beard, C. L. Gîjiu, D. Dinculescu and T. J. Schmidt, *Renew. Sustain. Energy Rev.*, 2022, **154**, 111807.
167 T. Alerte, J. P. Edwards, C. M. Gabardo, C. P. O'Brien, A. Gaona, J. Wicks, A. Obradović, A. Sarkar, S. A. Jaffer, H. L. MacLean, D. Sinton and E. H. Sargent, *ACS Energy Lett.*, 2021, **6**, 4405–4412.
168 J. Zhang, W. Luo and A. Züttel, *J. Catal.*, 2020, **385**, 140–145.
169 W. Sheng, Z. Zhuang, M. Gao, J. Zheng, J. G. Chen and Y. Yan, *Nat. Commun.*, 2015, **6**, 5848.
170 M. Bernt, A. Siebel and H. A. Gasteiger, *J. Electrochem. Soc.*, 2018, **165**, F305–F314.
171 J. Herranz, A. Pătru, E. Fabbri and T. J. Schmidt, *Curr. Opin. Electrochem.*, 2020, **23**, 89–95.
172 N. Hales, T. J. Schmidt and E. Fabbri, *Curr. Opin. Electrochem.*, 2023, **38**, 101231.
173 X. Ren, Y. Dai, X. Wen, B. Guo, C. Shi, X. Huang, Y. Guo and S. Li, *Adv. Sustain. Syst.*, 2024, **8**, 2300379.
174 P. Wei, H. Li, L. Lin, D. Gao, X. Zhang, H. Gong, G. Qing, R. Cai, G. Wang and X. Bao, *Sci. China Chem.*, 2020, **63**, 1711–1715.
175 Y. Xu, F. Li, A. Xu, J. P. Edwards, S.-F. Hung, C. M. Gabardo, C. P. O'Brien, S. Liu, X. Wang, Y. Li, J. Wicks, R. K. Miao, Y. Liu, J. Li, J. E. Huang, J. Abed, Y. Wang, E. H. Sargent and D. Sinton, *Nat. Commun.*, 2021, **12**, 2932.
176 L. Yuan, S. Zeng, X. Zhang, X. Ji and S. Zhang, *Mater. Rep. Energy*, 2023, **3**, 100177.
177 M. Mandal, *ChemElectroChem*, 2021, **8**, 1448–1450.
178 B. Siritanaratkul, P. K. Sharma, E. H. Yu and A. J. Cowan, *Adv. Mater. Interfaces*, 2023, **10**, 2300203.
179 B. Siritanaratkul, M. Forster, F. Greenwell, P. K. Sharma, E. H. Yu and A. J. Cowan, *J. Am. Chem. Soc.*, 2022, **144**, 7551–7556.
180 K. Xie, R. K. Miao, A. Ozden, S. Liu, Z. Chen, C.-T. Dinh, J. E. Huang, Q. Xu, C. M. Gabardo, G. Lee, J. P. Edwards, C. P. O'Brien, S. W. Boettcher, D. Sinton and E. H. Sargent, *Nat. Commun.*, 2022, **13**, 3609.
181 R. Fischer, M. Dessiex, F. Marone and F. Buchi, *ACS Appl. Energy Mater.*, 2024, **7**, 3590–3601.
182 J. Kwen, T. J. Schmidt and J. Herranz, *ACS Appl. Energy Mater.*, 2025, **8**, 4152–5165.
183 M. A. Blommaert, R. Sharifian, N. U. Shah, N. T. Nesbitt, W. A. Smith and D. A. Vermaas, *J. Mater. Chem. A*, 2021, **9**, 11179–11186.
184 Y. Li, D. Zhou, Z. Yan, R. Goncalves, D. Salvatore, C. Berlinguette and T. Mallouk, *ACS Energy Lett.*, 2016, **1**, 1149–1153.
185 D. Vermaas and W. Smith, *ACS Energy Lett.*, 2016, **1**, 1143–1148.
186 B. Pribyl-Kranewitter, A. Beard, T. Schuler, N. Diklic and T. J. Schmidt, *J. Electrochem. Soc.*, 2021, **168**, 043506.
187 J. Disch, S. Ingenhoven and S. Vierrath, *Adv. Energy Mater.*, 2023, **13**, 2301614.
188 G. Li, L. Huang, C. Wei, H. Shen, Y. Liu, Q. Zhang, J. Su, Y. Song, W. Guo, X. Cao, B. Zhong, M. Robert and R. Ye, *Angew. Chem., Int. Ed.*, 2024, **63**, e202400414.
189 M. Wrobel, S. Kriescher, T. Schiffer, R. Keller and M. Wessling, *Chem. Eng. J.*, 2023, **474**, 145335.
190 C. O'Brien, R. Miao, A. Zeraati, G. Lee, E. Sargent and D. Sinton, *Chem. Rev.*, 2024, **124**, 3648–3693.
191 S. Liang, N. Altaf, L. Huang, Y. Gao and Q. Wang, *J. CO2 Util.*, 2020, **35**, 90–105.
192 J. S. Diercks, B. Pribyl-Kranewitter, J. Herranz, P. Chauhan, A. Faisnel and T. J. Schmidt, *J. Electrochem. Soc.*, 2021, **168**, 064504.
193 J. Durst, A. Rudnev, A. Dutta, Y. Fu, J. Herranz, V. Kaliginedi, A. Kuzume, A. Permyakova, Y. Paratcha, P. Broekmann and T. J. Schmidt, *Chimia*, 2015, **69**, 769.
194 P. X. Liu, L. W. Peng, R. N. He, L. L. Li and J. L. Qiao, *J. Electrochem.*, 2022, **28**, 2104231.
195 R. He, N. Xu, I. M. ul Hasan, L. Peng, L. Li, H. Huang and J. Qiao, *EcoMat*, 2023, **5**, e12346.
196 T. Möller, T. N. Thanh, X. Wang, W. Ju, Z. Jovanov and P. Strasser, *Energy Environ. Sci.*, 2021, **14**, 5995–6006.
197 X. Zhang, Y. Wang, M. Gu, M. Wang, Z. Zhang, W. Pan, Z. Jiang, H. Zheng, M. Lucero, H. Wang, G. E. Sterbinsky, Q. Ma, Y.-G. Wang, Z. Feng, J. Li, H. Dai and Y. Liang, *Nat. Energy*, 2020, **5**, 684–692.
198 J. Su, J.-J. Zhang, J. Chen, Y. Song, L. Huang, M. Zhu, B. I. Yakobson, B. Z. Tang and R. Ye, *Energy Environ. Sci.*, 2021, **14**, 483–492.
199 Z. Chen, X. Zhang, W. Liu, M. Jiao, K. Mou, X. Zhang and L. Liu, *Energy Environ. Sci.*, 2021, **14**, 2349–2356.
200 Y. Li, N. M. Adli, W. Shan, M. Wang, M. J. Zachman, S. Hwang, H. Tabassum, S. Karakalos, Z. Feng, G. Wang, Y. C. Li and G. Wu, *Energy Environ. Sci.*, 2022, **15**, 2108–2119.
201 X. Wang, Z. Wang, F. P. García de Arquer, C.-T. Dinh, A. Ozden, Y. C. Li, D.-H. Nam, J. Li, Y.-S. Liu, J. Wicks, Z. Chen, M. Chi, B. Chen, Y. Wang, J. Tam, J. Y. Howe, A. Proppe, P. Todorović, F. Li, T.-T. Zhuang, C. M. Gabardo, A. R. Kirmani, C. McCallum, S.-F. Hung, Y. Lum, M. Luo, Y. Min, A. Xu, C. P. O'Brien, B. Stephen, B. Sun, A. H. Ip, L. J. Richter, S. O. Kelley, D. Sinton and E. H. Sargent, *Nat. Energy*, 2020, **5**, 478–486.
202 P. Wang, H. Yang, C. Tang, Y. Wu, Y. Zheng, T. Cheng, K. Davey, X. Huang and S.-Z. Qiao, *Nat. Commun.*, 2022, **13**, 3754.

203 C. Peng, S. Yang, G. Luo, S. Yan, M. Shakouri, J. Zhang, Y. Chen, W. Li, Z. Wang, T.-K. Sham and G. Zheng, *Adv. Mater.*, 2022, **34**, 2204476.

204 F. P. García de Arquer, C.-T. Dinh, A. Ozden, J. Wicks, C. McCallum, A. R. Kirmani, D.-H. Nam, C. Gabardo, A. Seifitokaldani, X. Wang, Y. C. Li, F. Li, J. Edwards, L. J. Richter, S. J. Thorpe, D. Sinton and E. H. Sargent, *Science*, 2020, **367**, 661–666.

205 W. Ma, S. Xie, T. Liu, Q. Fan, J. Ye, F. Sun, Z. Jiang, Q. Zhang, J. Cheng and Y. Wang, *Nat. Catal.*, 2020, **3**, 478–487.

206 L. Zhang, X.-X. Li, Z.-L. Lang, Y. Liu, J. Liu, L. Yuan, W.-Y. Lu, Y.-S. Xia, L.-Z. Dong, D.-Q. Yuan and Y.-Q. Lan, *J. Am. Chem. Soc.*, 2021, **143**, 3808–3816.

207 Y. Wu, H. Rabiee, X. S. Zhao, G. Wang and Y. Jiang, *J. Mater. Chem. A*, 2024, **12**, 14206–14228.

208 C. P. O'Brien, R. K. Miao, A. Shayesteh Zeraati, G. Lee, E. H. Sargent and D. Sinton, *Chem. Rev.*, 2024, **124**, 3648–3693.

209 S. Vesztergom, A. Senocrate, Y. Kong, V. Kolivoska, F. Bernasconi, R. Zboray, C. Battaglia and P. Broekmann, *Chimia*, 2023, **77**, 104.

210 A. Reyes, R. Jansonius, B. Mowbay, Y. Cao, D. Wheeler, J. Chau, D. Dvorak and C. Berlinguette, *ACS Energy Lett.*, 2020, **5**, 1612–1618.

211 D. Wheeler, B. A. W. Mowbay, A. Reyes, F. Habibzadeh, J. He and C. Berlinguette, *Energy Environ. Sci.*, 2020, **13**, 5126–5134.

212 R. Garcia-Barros, M. Kelleners, L. Van Bemmel, T. van der Leegte, J. van der Schaaf and M. de Groot, *Electrochim. Acta*, 2024, **507**, 145161.

213 B. Endrodi, A. Samu, E. Kecsenovity, T. Halmágyi, D. Sebok and C. Janáky, *Nat. Energy*, 2021, **6**, 439–448.

214 Z. Liu, H. Yang, R. Kutz and R. Masel, *J. Electrochem. Soc.*, 2018, **165**, J3371.

215 Y. Xu, J. Edwards, R. Miao, J. Huang, C. Gabardo, C. O'Brien, J. Li, E. Sargent and D. Sinton, *ACS Energy Lett.*, 2021, **6**, 809–815.